



Structural and electrical dynamics of a grating-patterned triboelectric energy harvester with stick–slip oscillation and magnetic bistability

Huai Zhao · Huajiang Ouyang

Received: 30 August 2021 / Accepted: 11 January 2022 / Published online: 5 May 2022
© The Author(s) 2022, corrected publication 2022

Abstract The majority of research work on triboelectric energy harvesting is on material science, manufacturing and electric circuit design. There is a lack of in-depth research into structural dynamics which is crucial for power generation in triboelectric energy harvesting. In this paper, a novel triboelectric energy harvester with a compact structure working in sliding mode is developed, which is in the form of a casing and an oscillator inside. Unlike most sliding-mode harvesters using single-unit films, the proposed harvester utilizes grating-patterned films which are much more efficient. A bistable mechanism consisting of two pairs of magnets is employed for broadening the frequency bandwidth. A theoretical model is established for the harvester, which couples the structural dynamics domain and electrical dynamics domain. This paper presents the first study about the nonlinear structural dynamics of a triboelectric energy harvester with grating-patterned films, which is also the first triboelectric energy harvester integrating grating-patterned films with a bistable magnetic system for power performance enhancement. Theoretical studies are carried out from the perspectives of both structural and electrical dynamics. Surface charge density and segment configuration of the films affect whether the electrostatic force influences the structural

dynamics, which can be neglected under a low surface charge density. Differences in structural response and electrical output are found between a velocity-dependent model and Coulomb's model for modelling the friction in the triboelectric energy harvesting system. The bistable mechanism can effectively improve the output voltage under low-frequency excitations. Additionally, the output voltage can also be obviously enhanced through increasing the number of the hollowed-out units of the grating-patterned films, which also results in a slight decrease in the optimal load resistance of the harvester. These findings enable innovative designs for triboelectric energy harvesters and provide fabrication guidelines in practical applications.

Keywords Triboelectric energy harvesting · Grating-patterned film · Bistable mechanism · Friction

1 Introduction

1.1 Triboelectric energy harvesting

In recent decades, the progressive developments in the Internet of things (IoT) have driven up the demand for a variety of wireless electronics and wearable electronics. Batteries, as traditional power sources for those low-power electronics, have a limited life and

H. Zhao · H. Ouyang (✉)
School of Engineering, University of Liverpool,
Liverpool L69 3GH, UK
e-mail: h.ouyang@liverpool.ac.uk

stored electricity, which also bring about extra cost on maintenance and recycling. These have led to more interest in developing a sustainable, renewable and environmentally friendly substitute of energy supplies to self-powered systems. Among a variety of energy harvesting technologies, vibration energy harvesting is a promising and popular one. Piezoelectric energy harvesting and magnetoelectric energy harvesting, as two most common types of vibration-based energy harvesters, have been studied extensively. Since the first report of a triboelectric nanogenerator (TENG) proposed by Zhonglin Wang's group in 2012 [1], triboelectric energy harvesting has received more and more attention in recent years, which has displayed a great potential for harvesting mechanical energy utilizing organic and inorganic materials.

Triboelectric energy harvesters (TEHs) work through a conjunction of triboelectrification and electrostatic induction, resulting from vertical contact-separation or lateral sliding induced by external mechanical force between the contact surfaces of two distinct materials with opposite triboelectric polarities [2]. According to the working principle, TEHs are categorized in four basic modes, namely vertical contact-separation mode, lateral sliding mode, single electrode mode and freestanding mode. In contrast to classical piezoelectric energy harvesters (PEHs) and magnetoelectric energy harvesters (MEHs) using, respectively, polycrystal or single-crystal piezoelectric materials and magnets and coils, TEHs can utilize a huge variety of materials, from metals to polymers, to silk and to wood. The wide selection for materials endows triboelectric energy harvesters with obvious advantages, such as light weight, low cost, environmental friendliness, biocompatibility and versatility. Most importantly, TEHs work best under low frequencies, which are suitable for harvesting low-frequency energy from body motion [3, 4] and ocean wave (blue energy). Besides, some designs for wind energy [5–7] also exhibit good performance. The flexibility of some materials makes it feasible to integrate TEHs with textiles for wearable technology [8]. Those deformable and stretchable harvesters show a great potential in electronic skin, which has high competitiveness for next-generation energy, sensing and robotic applications [9]. In medical field, TEHs also make a great contribution, which can be integrated with a total knee replacement as a smart knee implant for routine monitoring without the need for

any external power source throughout the entire life [10, 11]. Due to the good linear relationship between the output voltage and external acceleration, TEHs can be used as self-powered acceleration sensors [12]. Additionally, TEHs can also be integrated with many other sensors, such as the wind speed detection sensor [13], the inertial motion sensor [14], the pressure mapping sensor [15] and human motion monitoring sensor [16]. Recently, a waterproof and breathable TEH was developed to drive a multifunctional plant sensor and transmit data remotely, which was attached to plant leaves conformally for harvesting energy from wind and raindrops [17]. Apparently, triboelectric energy harvesting has broad application prospects with distinct merits in energy harvesting.

Currently, most studies about triboelectric energy harvesting focus on material technology, surface technology, fabrication and experimental demonstrations of energy generation. Although the properties of triboelectric layers and manufacturing techniques are crucial for TEHs, since they directly affect the performance of practical applications. The structural dynamics involved is equally important, because the relative displacement between the surfaces of two distinct materials is the source of the generated power. For PEHs and MEHs, their structural behaviours have been investigated extensively. In the field of triboelectric energy harvesting, such studies targeting or involving dynamic behaviour of TEHs are fairly rare and far from deep. Nelson et al. [18] proposed a contact-separation-mode triboelectric energy harvester with a compressive axial force at one end of a beam, which allowed the harvesting system to be tuned to accommodate various vibration sources at low frequency. Fu et al. [19] studied the nonlinear dynamics of a freestanding-mode triboelectric energy harvester based on a three-degree-of-freedom vibro-impact oscillator and found that chatter and stick could improve the power output. These authors also investigated an improved harvester in the form of three parallel cantilever beams [20]. Both the structural response and output voltage of the harvester were found to increase linearly with excitation. Wang et al. [21] proposed a sliding-mode triboelectric energy harvester in combination with a quasi-zero-stiffness (QZS) mechanism. The QZS spring could produce quite low stiffness in a fairly large displacement region, which enhanced harvesting efficiency under ultra-low-frequency vibration. Based on a sliding-

mode triboelectric energy harvester consisting of a cantilever beam, a tip mass and three magnets, multistable dynamics [22] and the effect of electrical properties for triboelectric films on vibrations [23] were investigated numerically. A galloping triboelectric energy harvester with two flexible beams was developed for wind energy [6]. It was found higher wind speed produced a larger vibration velocity, resulting in larger contact force, which increased the microscale contact area and consequently improved surface charge density.

1.2 Power boosting strategies

Improving harvesting efficiency is always a demand for all types of energy harvesters. In terms of triboelectric energy harvesting, a number of methods from different perspectives have been proposed for power enhancement. Herein, some power boosting strategies are categorized and briefly reviewed.

Triboelectrification is closely related to the electric properties of triboelectric materials. Thus, in the aspect of material science, the direct way to enhance the charge transferring efficiency is to improve the properties of materials. Via incorporating ZnO nanorods [24] or electrospun MXene ($\text{Ti}_3\text{C}_2\text{T}_x$) [25] into polyvinylidene fluoride (PVDF) polymer, triboelectrification can be considerably enhanced. Functionalizing polydimethylsiloxane (PDMS) with polystyrene (PS) and pentafluorostyrene (PPFS) [26] is also an effective way.

Besides material properties, the surface condition of triboelectric layers also greatly affects the charge transferring process. In principle, the larger the contact area, the more the transferred charges, and the higher the output power. Therefore, in the field of surface science, nanowires [27] or patterned arrays [28, 29] are introduced on the contact surfaces of triboelectric layers, which can increase the contact area in micro/nanoscale and consequently improve the electric performance of TEHs.

A distinct characteristic of TEHs is high internal electrical impedance, which means that a high load resistance is usually required to match the high internal impedance. This also results in low output current in load circuits. From the perspective of electric circuits, it is necessary to reduce the internal impedance and increase the output current. Opposite needles enclosed in an inert atmosphere were utilized

to reduce the internal impedance of TEHs when connected in series with harvesters, which was proved to improve the maximum power by 330.76% [30]. Additionally, integrating a number of sub-harvesters in a single harvester design and synchronizing the outputs of those sub-harvesters can potentially enhance the instantaneous output current of energy harvesting devices [31].

In the structure aspect, the power of TEHs can be promoted through improving the geometric shape of films or configuration of harvesters. Firstly, for the films, its geometric shape has a great impact on the overlapping area between two distinct layers in sliding-mode TEHs, which accordingly affect the power generation. In most sliding-mode harvesters, such as the harvester in Ref. [22], their films are in the form of a single unit. The output voltage from this kind of films usually is not very high under small-amplitude vibrations. Grating-patterned films, as a kind of advanced film design based on the single-unit films, can improve in-plane charge separation cycles, thus bringing about higher power [2]. The electric dynamics of the grating-patterned films has been investigated, but the study about this kind of films in vibration is absent, especially in structural dynamics. Secondly, regarding the harvester configuration, structural nonlinearity is often introduced into harvesting systems to broaden frequency bandwidth and improve harvesting efficiency. Bistable mechanism (snap-through mechanism), as one of the nonlinear mechanisms, has been extensively studied and widely used in piezoelectric energy harvesting [32, 33] and magnetoelectric energy harvesting [34, 35]. However, in triboelectric energy harvesting, the bistable mechanism is not common and was reported in only several publications. Fu et al. [22] investigated the magnetic bistability in cantilever-beam-based harvesters through numerical simulations. Deng et al. [36] utilized permanent magnets and springs in a TEH as a bistable structure for broadband energy harvesting under low frequencies. Hassani et al. [37] developed a bistable actuator to empty the bladder, with which a flexible triboelectric nanogenerator sensor was integrated for detecting the fullness of the bladder. Regarding the research status of TEHs, there is still a large scope for the integration between the bistable mechanism and the triboelectric energy harvesting.

1.3 Objectives of this study

In this study, a triboelectric energy harvester in the form of a compact closed casing working in lateral sliding mode is developed for vibration energy. In contrast to traditional single-unit films which have been widely studied, grating-patterned films, as a kind of advanced film structure, are utilized in the proposed harvester for power enhancement. Two pairs of magnets, serving as a bistable mechanism, are employed for broadening frequency bandwidth and further enhancing harvesting efficiency. The harvester can be utilized to power wireless structural health monitoring sensors on vibrating structures such as bridges or wind turbines. This paper aims to investigate the structural and electrical dynamics of the harvester based on the grating-patterned films and the bistable mechanism. It makes the following scientific contributions to triboelectric energy harvesting:

- (1) This paper presents a novel triboelectric energy harvester in sliding mode. It is the first harvester combining grating-patterned films and a bistable mechanism, which provide a dual enhancement effect for triboelectric energy harvesting.
- (2) A theoretical model coupling the structural dynamic domain and electric dynamic domain is established, which is the first study of the nonlinear structural dynamics of a triboelectric energy harvester with grating-patterned films.
- (3) The friction in the harvester is modelled through a velocity-dependent model, which is compared with the traditional Coulomb's model.
- (4) The effect of grating segmentation for films is investigated and compared with the traditional single-unit films in nonlinear vibration for demonstrating the superiority of the grating-patterned films.

The outline for the rest of this paper is as follows: Sect. 2 describes the configuration of the proposed harvester and the basic working mechanism of sliding-mode triboelectric energy harvesting. Section 3 and Sect. 4 present the structural dynamics model and the electrical dynamics model of the harvester, respectively. In Sect. 5, a number of issues are investigated theoretically, including the effect of the electrostatic force, the comparison between the velocity-dependent model and Coulomb's model of friction, the effects of

the potential wells, the excitation level and the grating segmentation for films and the overall electric performance. Finally, the main conclusions of this study are drawn in Sect. 6.

2 Structure design

The proposed harvester is illustrated in Fig. 1a and b, which is integrated into a cuboid casing with a compact structure. The casing consists of a top plate, a frame and a bottom plate, in which a cuboid oscillator can move longitudinally. The two ends of the oscillator are connected with the frame by two linear compression springs, which provide restoring forces during oscillation. Two pairs of repulsive magnets sit symmetrically at two sides of the oscillator, as shown in Fig. 1c. Two of the magnets are attached with the oscillator and the other two are fixed on the frame. The two pairs of magnets provide nonlinear forces and serve as a bistable mechanism, which is able to broaden the responsive frequency bandwidth and enhance the efficiency of the harvester. Both the top surface and bottom surface of the oscillator are covered with a copper film and then a dielectric film made of polytetrafluoroethylene (PTFE) as the outside surface of the oscillator, as shown in Fig. 1d. Correspondingly, the bottom surface of the top plate and the top surface of the bottom plate are covered with a copper film, respectively. The dielectric films on the oscillator contact with the metal films on the top plate and bottom plate. As a consequence, the proposed harvester has two sub-harvesters in in-plane sliding mode, one of which is on the top and the other one is on the bottom. All the metal films and dielectric films have a grating structure with the same pattern, the detailed information of which will be given in Sect. 5.5.

For each sub-harvester, the two sheets of metal films work as two electrodes. When the harvester is exposed to horizontal external excitations, the oscillator is able to vibrate inside the casing and electricity can be generated in lateral sliding mode, whose working mechanism is schematically depicted in Fig. 2. In the initial position (Fig. 2-I), the two electrodes fully overlap. Due to the distinct electric polarities in the ability to attract electrons of the metal film and the dielectric film, triboelectrification takes place and electron transfer from the single plate-

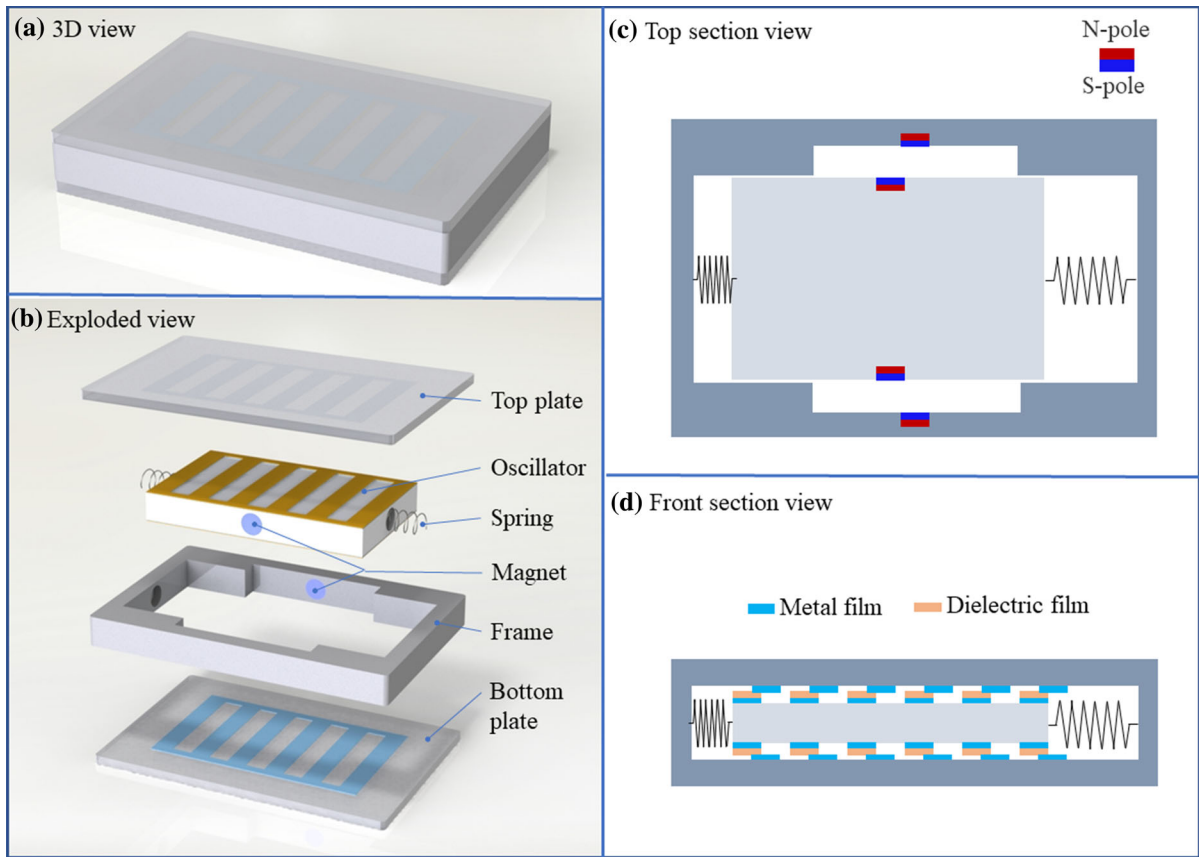


Fig. 1 Configuration of the proposed harvester

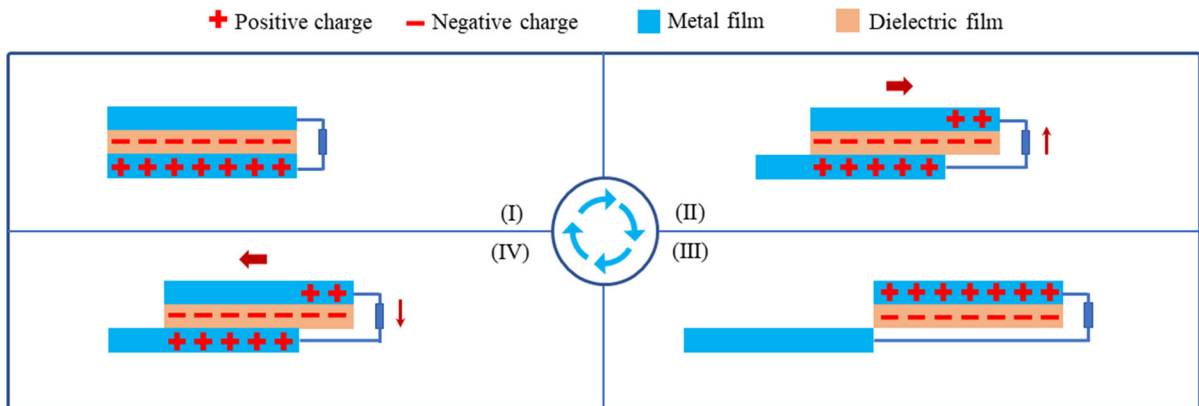


Fig. 2 Working mechanism of sliding mode

attached metal film to the dielectric film, resulting in net positive charges on the single metal film and net negative charges with equal density on the dielectric film. With the vibration of the oscillator, the electrode attached with the dielectric film slides out of the single

metal film (Fig. 2-II), and an in-plane charge separation is initiated due to the decrease in contact surface area. An electric potential difference is induced because of the separated charges, which is able to drive a current flow through an external load to

generate an electric potential drop that cancels the tribo-charge-induced potential. When the electrode just fully slides out of the other electrode (Fig. 2-III), the electric potential difference reaches a maximum. Subsequently, when the movable electrode slides backwards (Fig. 2-IV), the separated charges begins to get in contact again and an opposite current flow is generated through the load circuit. In this entire cycle, the current flow changes direction with the outwards and inwards sliding motion. Therefore, an alternating current will be generated during continuous oscillation.

3 Structural dynamics model

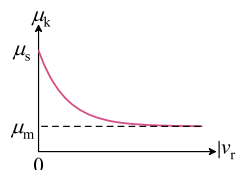
3.1 Friction law

Friction plays a significant role in sliding-mode triboelectric energy harvesters, which affects both the response in structural dynamics domain and charge transferring process in electrical dynamics domain. In the proposed harvester, during working, dry friction exists between the bottom surface of the oscillator and the bottom plate, and between the top surface of the oscillator and the top plate. A velocity-dependent friction model is utilized here, in which the friction is related to the relative velocity v_r between the oscillator and the casing.

When the relative velocity $v_r \neq 0$, a kinetic friction force acts on the oscillator. Herein, the velocity-dependent model (also called exponential-type model) is employed, in which the coefficient of kinetic friction asymptotically decreases to a constant level as the relative velocity increases, as shown in Fig. 3. This type of friction model is commonly used for contact between solid surfaces in dry conditions [38, 39], and the coefficient of kinetic friction can be expressed as

$$\mu_k(v_r) = \mu_m + (\mu_s - \mu_m)e^{-\alpha|v_r|} \tag{1}$$

Fig. 3 Velocity-dependent model



where μ_m denotes the minimum coefficient of kinetic friction and α is a tuning parameter used to control the negative slope of the coefficient curve. μ_s denotes the coefficient of static friction.

Therefore, the kinetic friction force follows

$$F_k = -sgn(v_r)\mu_k(v_r)F_n \tag{2}$$

where $sgn(\cdot)$ is the signum function. F_n is the total normal force between the oscillator and the casing, which can be written as

$$F_n = (1 + \varepsilon)mg \tag{3}$$

where m is the mass of the slider. In consideration of the fact that the top plate of the casing may apply a slight compressive force normally on the slider due to errors of manufacture and assembly which affects the friction, a modification coefficient ε is introduced to modify the total normal force between the oscillator and the casing.

The static friction force is presented on the oscillator while $v_r = 0$, and the maximal static friction force can be obtained from

$$F_s^{max} = \mu_s F_n \tag{4}$$

3.2 Dynamic response with stick–slip

It is assumed that the casing of the harvester is fixed to an ideal vibration source with a prescribed motion $x_c = A\sin(\omega t)$, in which A and ω denote the amplitude and radian frequency of excitation. The structural dynamics model is illustrated in Fig. 4. The governing equation of motion for the oscillator depends on the relative velocity v_r between the oscillator and the casing. When $v_r \neq 0$, slip motion takes place and the motion of the oscillator is governed by

$$m\ddot{x}_m = F_k - F_r + F_{mag} + 2F_e \tag{5}$$

where x_m is the absolute displacement of the oscillator along X -axis. $F_r = 2k(x_m - x_c)$ is the restoring force from the springs, in which k denotes the stiffness of the springs on each side. F_{mag} and F_e represents the magnetic force and electrostatic force on the

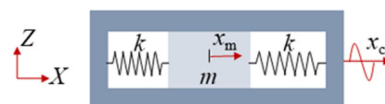


Fig. 4 Schematic of the structural dynamics model

oscillator, which will be detailed in the subsequent paragraphs.

By introducing the relative displacement $x = x_m - x_c$ between the oscillator and the casing, then the relative velocity can be expressed as $v_r = \dot{x}_m - \dot{x}_c = \dot{x}$. By substituting $x = x_m - x_c$ and $v_r = \dot{x}$ into Eq. 5, it can be re-written as

$$m\ddot{x} + \text{sgn}(\dot{x})\mu_k F_n = mA\omega^2 \sin(\omega t) - 2kx + F_{\text{mag}} + 2F_e \tag{6}$$

The terms on the right-hand side in the equation above can be regarded as a varying force $F(t, Q)$ depending on time t and charge Q , written as

$$F(t, Q) = mA\omega^2 \sin(\omega t) - 2kx + F_{\text{mag}} + 2F_e(Q) \tag{7}$$

Stick motion occurs during $v_r = 0$ and $|F(t, Q)| \leq F_s^{\text{max}}$, and the motion of the oscillator follows

$$\dot{x} = 0, \ddot{x} = 0, \tag{8}$$

Two pairs of neodymium disc magnets are located symmetrically about the X -axis in the harvester, which have the same magnetic dipole moment M ($M = 0.1 \text{ Wb}\cdot\text{m}$ is utilized in this work). Figure 5 illustrates the magnetic force between the two magnets versus the gap obtained from a simplified magnetic dipole model [40, 41]. It can be seen that when the gap between the two magnets exceeds approximately 0.015 m, the magnetic force between the two magnets is nearly zero. And the width of the oscillator is larger than 0.015 m in this work. Therefore, the magnetic fields of the two magnets at one side of the oscillator can be reasonably ignored at the other side of the oscillator. Here, one pair of magnets are taken as an example for

detailed formulation. Figure 5 (b) shows the relative locations for the pair of magnets, where the magnet fixed with the frame is referred to as magnet A and the other magnet fixed on the oscillator is referred to as magnet B. The magnetic repulsive force is characterized by employing the simplified magnetic dipole model, expressed as

$$\mathbf{F}_{\text{mag}} = \frac{3\mu_0 M^2}{4\pi r^4} (2\mathbf{e}_x \sin\theta + 2\mathbf{r} - 5\mathbf{r} \sin^2\theta) \tag{9}$$

where μ_0 is the magnetic permeability in a classical vacuum, M is the magnetic dipole moments for magnet A and magnet B, and \mathbf{e}_x and \mathbf{r} are unit vectors, whose directions are illustrated in Fig. 5b. r represents the distance between the centres of magnet A and magnet B, which is expressed as

$$r = \sqrt{d^2 + x^2} \tag{10}$$

in which d is the gap between the centres of magnet A and magnet B along the Y -axis. θ is an angle between vector \mathbf{r} and the Y -axis, which can be obtained by

$$\theta = \tan^{-1} \frac{x}{d} \tag{11}$$

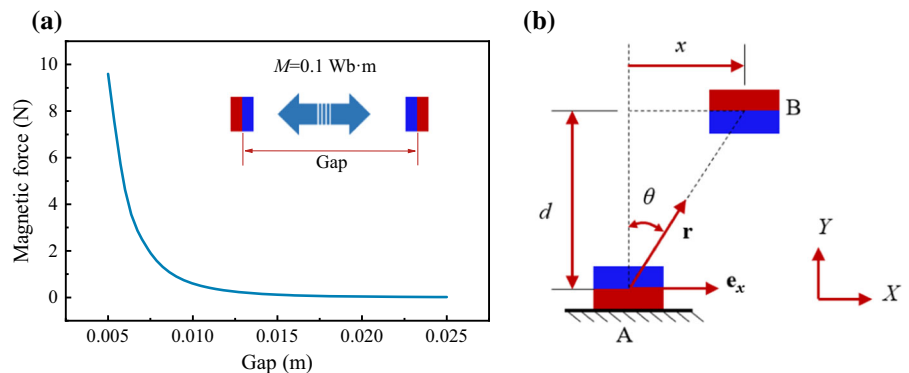
Therefore, the total magnetic force on the oscillator along the X -axis can be shown as

$$F_{\text{mag}} = 2\mathbf{e}_x \mathbf{F}_{\text{mag}} = \frac{3\mu_0 M^2}{2\pi r^4} (4\sin\theta - 5\sin^3\theta) \tag{12}$$

4 Electrical dynamics model

A triboelectric energy harvester can be equivalized by a series connection of an equivalent capacitor C_e and an open-circuit voltage source V_{oc} [42, 43], as shown

Fig. 5 Magnetic force (a) and relative locations (b)



in Fig. 6a. In this work, the equivalent capacitance and open-circuit voltage are based on a premise that the area dimension of the units on the films is sufficiently greater than the thickness of the films so that the edge effect between the electrodes can be ignored [2].

The proposed harvester consists of two sub-harvesters on the top and bottom, which have the same electric characteristic. For each sub-harvester, the equivalent capacitance and open-circuit voltage can be derived as

$$A_1 = \begin{cases} w_0(\delta - x_0)(n - n_0 + 1) + (l - 2\delta n_0 - x_0)(w - w_0), & x_0 \in [0, \delta] \\ w_0(x_0 - \delta)(n - n_0) + (l - 2\delta n_0 - x_0)(w - w_0), & x_0 \in (\delta, 2\delta) \end{cases} \tag{15}$$

$$A_2 = \begin{cases} w_0\delta n_0 + w_0x_0(n - n_0 + 1) + (2\delta n_0 + x_0)(w - w_0), & x_0 \in [0, \delta] \\ w_0\delta(n_0 + 1) + w_0(2\delta - x_0)(n - n_0) + (2\delta n_0 + x_0)(w - w_0), & x_0 \in (\delta, 2\delta) \end{cases} \tag{16}$$

$$C_e = \frac{\epsilon_0 \epsilon_r A_1}{t_h} \tag{13}$$

$$V_{oc} = \frac{\sigma A_2 t_h}{\epsilon_0 \epsilon_r A_1} \tag{14}$$

where ϵ_0 and ϵ_r are absolute dielectric permittivity of classical vacuum and the relative permittivity of the dielectric film, respectively. t_h denotes the thickness of the dielectric film and σ is the surface charge density. A_1 is the overlapping area between the dielectric film and the single metal film during slider oscillation. A_2 is the rest of the dielectric film apart from the overlapping part. The metal films and the dielectric film have the same grating pattern, as shown in Fig. 6b. n represents the number of the hollowed-out units. $\delta = \frac{l}{2n+1}$ is the width of a single unit, in

which l is the length of the whole film. Both A_1 and A_2 are functions of the relative displacement x . By introducing $x_0 = \text{rem}(|x|, 2\delta)$ and $n_0 = \text{floor}(\frac{|x|}{2\delta})$ where $\text{rem}(\cdot)$ and $\text{floor}(\cdot)$ are the functions of returning the remainder and the integer quotient, one can get A_1 and A_2 as

in which w and w_0 denote the width of the whole

film and the length of the hollowed-out units, respectively.

In order to assess the electric performance of the harvester numerically, each sub-harvester is wired with a load resistor R . Note that in practical applications, the two sub-harvesters can be connected in parallel to power a load circuit. The relationship between the voltage V across the resistor R in an outer circuit and the amount of transferred charges Q between the two electrodes can be given by

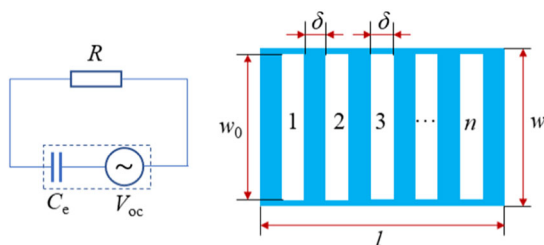
$$V = -\frac{Q}{C_e} + V_{oc} \tag{17}$$

By applying Ohm's law, namely $V = RI = R \frac{dQ}{dt}$ (I denotes the current), the electric differential equation can be derived as

$$R \frac{dQ}{dt} + \frac{Q}{C_e} - V_{oc} = 0 \tag{18}$$

Under the initial condition $Q = 0$ at $t = 0$, the equation above can be solved, and then, the transferred charges Q and the voltage V across the resistor R can be obtained by

$$Q(t) = \frac{1}{R} e^{-\frac{t}{RC_e}} \int_0^t V_{oc} e^{\frac{t}{RC_e}} \frac{1}{C_e} dt \tag{19}$$



(a) Equivalent electric circuit (b) Pattern of triboelectric films

Fig. 6 Electrical model

$$V(t) = V_{oc} - \frac{1}{RC_e} e^{-\frac{t}{RC_e}} \int_0^t V_{oc} e^{\frac{t}{RC_e}} dt \quad (20)$$

During stick, the transferred charges remain unchanged, thus

$$Q = Q(t_{st}), \frac{dQ}{dt} = 0 \quad (21)$$

where t_{st} is the time instant at the onset of stick motion and $Q_i(t_{st})$ is the corresponding transferred charges.

The electrostatic force may affect the structural response of the oscillator, which should be taken into consideration. The electrostatic force on the oscillator can be calculated by differentiating the total potential energy of the capacitive system with respect to the position of the movable electrode [44, 45], which can be obtained as

$$F_e = \begin{cases} \frac{Q^2 t_h [w_0(n - n_0 + 1) + (w - w_0)]}{2\epsilon_0 \epsilon_r A_1^2}, & x \geq 0, x_0 \in [0, \delta] \\ -\frac{Q^2 t_h [w_0(n - n_0 + 1) + (w - w_0)]}{2\epsilon_0 \epsilon_r A_1^2}, & x < 0, x_0 \in [0, \delta] \\ -\frac{Q^2 t_h [w_0(n - n_0) - (w - w_0)]}{2\epsilon_0 \epsilon_r A_1^2}, & x \geq 0, x_0 \in (\delta, 2\delta) \\ \frac{Q^2 t_h [w_0(n - n_0) - (w - w_0)]}{2\epsilon_0 \epsilon_r A_1^2}, & x < 0, x_0 \in (\delta, 2\delta) \end{cases} \quad (22)$$

5 Numerical studies

In this paper, the proposed harvester exhibits non-smooth dynamics in the structural dynamic domain due to the stick–slip motion induced by the friction, and stiffness in the electrical model. The trapezoidal rule combined with backward differentiation formula is employed to solve the electromechanical coupling

model, which is suitable for solving stiff systems. For capturing the transition time instants between stick and slip, the bisection method is utilized, during which the tolerance is set to 10^{-4} . Unless particularly stated, all the parameters of the harvester used in simulations can be seen in Table 1.

5.1 Electrostatic force

The structural dynamic domain and the electrical dynamic domain are coupled by the electrostatic force between two electrodes resulting from triboelectrification, which may affect the dynamic behaviour of the harvester. For investigating the effect of the electrostatic force, the coupled model and an uncoupled model with and without consideration of the electrostatic force are compared. Note that the term of the electrostatic force should be removed from Eq. (6) in the uncoupled model. To simplify the comparison, all the magnets are removed from the harvester. The tuning parameter $\alpha = 30$ is used here, and other parameters utilized in this section are shown in Table 1.

Figure 7a illustrates the root-mean-square (RMS) displacements of the oscillator under discrete numerical frequency sweep from 8 to 16 Hz with an excitation amplitude of 0.0008 m based on the coupled and uncoupled models. The displacements are expected to be different if the electrostatic force has an obvious impact in the structural dynamic domain. Nevertheless, as observed, the frequency responses of the coupled and uncoupled models are almost identical, which means the effect of the electrostatic force is neglectable in the mechanical model. Additionally, as shown in Fig. 7a, stick–slip vibration with a small amplitude takes place at 10.6 Hz. When the excitation

Table 1 Design parameters of the harvester

Parameter	Value	Parameter	Value
m	0.03 kg	ϵ_0	8.85×10^{-12} F/m
k	60 N/m	ϵ_r	2.05
μ_m	0.2	t_h	30 μm
μ_s	0.3	σ	20 $\mu\text{C}/\text{m}^2$
α	30	l	40 mm
ϵ	0.05	w	30 mm
M	0.1 Wb·m	w_0	25 mm
μ_0	$4\pi \times 10^{-7}$ Wb/(A·m)	R	10 M Ω
n	4		

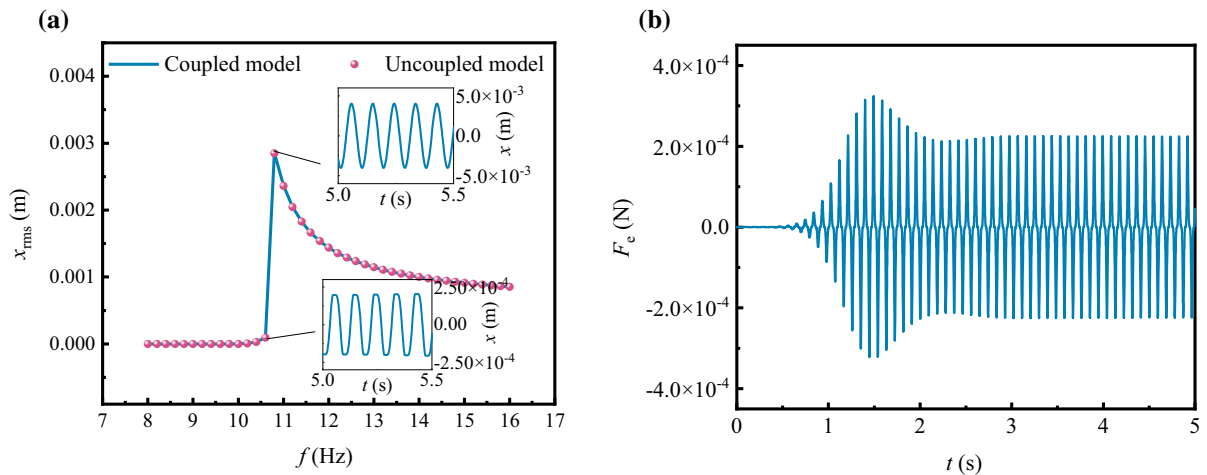


Fig. 7 Comparison of the displacements with and without consideration of the electrostatic force

frequency reaches 10.8 Hz, pure slip motion with a large amplitude occurs. The frequency response of the oscillator experiences a sharp jump due to friction. For further investigation, the electrostatic force at 10.8 Hz is plotted in Fig. 7b. It can be seen that the magnitude of the electrostatic force is quite small, which can be ignored safely under the certain conditions.

The materials of the films may affect the electrostatic force as different materials have distinct electric polarities, consequently resulting in different surface charge densities on the contact surfaces. The surface charge density plays a significant role in power generation. In theory, the further away two materials are from each other on triboelectric series, the higher

the surface charge density, and the more the charge transferred [2]. Figure 8 (a) shows the frequency response under different values of surface charge density when $n = 4$. It can be seen that the increase in the surface charge density reduces the vibration amplitude, because a higher surface charge density results in a stronger electric field and a larger electrostatic force, which acts like structural damping. A similar conclusion can be seen in Ref. [23]. When the surface charge density varies in a relatively low range, such as from 1 to $40 \mu\text{C}/\text{m}^2$, the decrease in vibration amplitude is very small, and the effect of the electrostatic force on structural response can be ignored reasonably. A fairly large surface charge

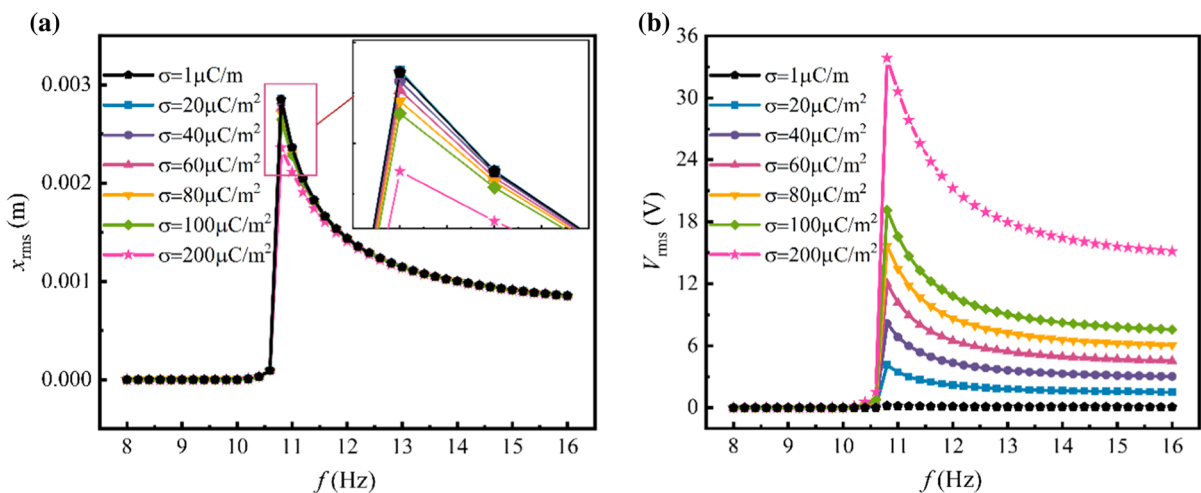


Fig. 8 Comparison of the displacement (a) and output voltage (b) under different surface charge densities

density (such $200 \mu\text{C}/\text{m}^2$) brings about obvious reduction of the response. In that case, the effect of the electrostatic force should not be ignored any longer. Although a larger surface charge density results in smaller vibration amplitudes, the output voltage is improved dramatically with the increase in the surface charge density, as shown in Fig. 8b. For most common materials, the surface charge density is not very high. A way to increase the surface charge density is to improve the electric polarity (by using functionalized materials) or surface condition of the films (by using micro- and nanopatterning films). This is the reason why functionalized materials and nanopatterning films have gained great attention in TEH, as mentioned in the Introduction section, which contribute to increase the surface charge density and effectively enhance the output performance of triboelectric energy harvesters.

Besides the materials of the films, the segment configuration of the films may also have an impact on the electrostatic force, accordingly affecting the structural response of the oscillator. Figure 9a illustrates the RMS displacement of the oscillator when the surface charge density σ is $20 \mu\text{C}/\text{m}^2$ under three different segment configurations, namely $n = 0, 4$ and 8 . The results indicate that the vibration amplitudes are nearly the same under different segment configurations with this low level of charge density. Nevertheless, when the surface charge density increases to a large level, such as $\sigma = 200 \mu\text{C}/\text{m}^2$, the situation becomes quite different, as shown in Fig. 9b. The increase of segment number n results in a decrease in

vibration amplitude. According to Eq. (22), it can be seen that the electrostatic force is related to the transferred charge Q and segment number n . When the surface charge density is at a low level, the transferred charge Q is always low under different segment configurations, resulting in a weak electrostatic force. Thus, the effect of the electrostatic force on structural response is not obviously influenced by the segment configuration. However, a large surface charge density results in much more charges available during transfer. In that case, due to the enhanced charge transferring efficiency resulting from the increase of the segment number, which will be presented in Sect. 5.5, the transferred charge Q is increased dramatically, bringing about a significant increase in the electrostatic force, and consequently reducing the vibration amplitude.

In this paper, the PTFE film and copper film are common materials, which have a relatively low surface charge density. Based on some experiment results [46], a surface charge density of $20 \mu\text{C}/\text{m}^2$ is utilized for the materials in this paper. Accordingly, the electrostatic force is ignored for the proposed harvester. Then, the structural dynamics model and the electrical dynamics model can be treated as uncoupled from each other. As mentioned in Sect. 4, the equivalent circuit of a triboelectric energy harvester is a series connection of a capacitor and a voltage source, which are functions of the relative displacement of the oscillator. Therefore, an equivalent circuit model for a sub-harvester of the proposed harvester is established in Simulink software package, in which the structural

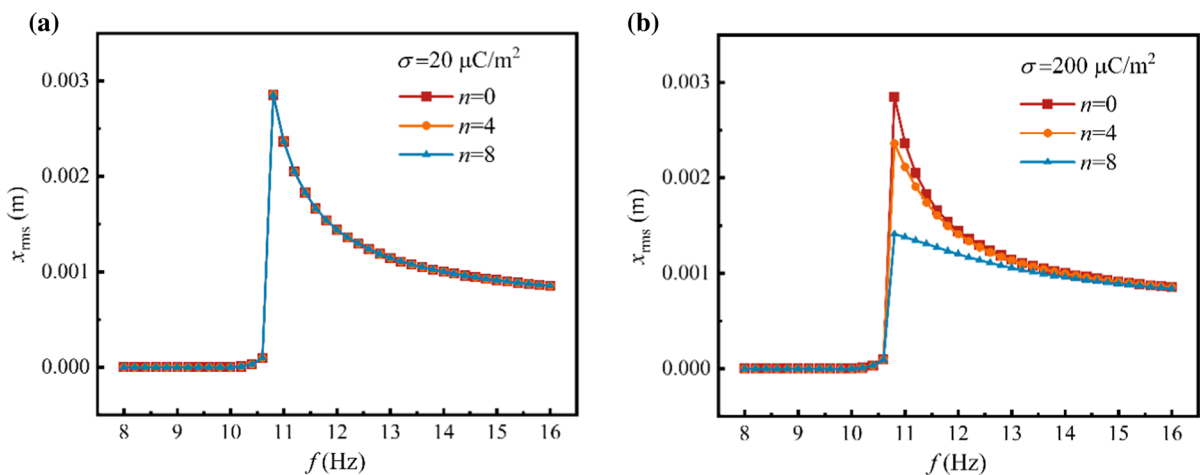


Fig. 9 Comparison of the displacements under different segment configurations

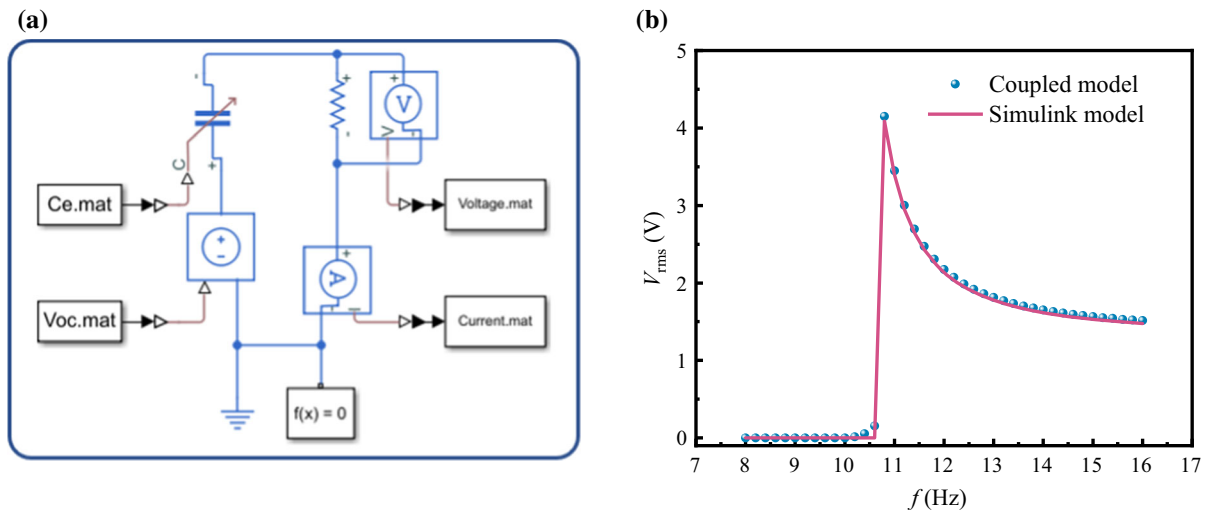


Fig. 10 Simulink model (a) of a sub-harvester and comparison of output voltages (b) between the coupled model and Simulink model

response of the oscillator determined in the structural dynamics is utilized as input data for the electrical model, as illustrated in Fig. 10a. The RMS voltages across the resistor in the coupled model and the Simulink model under frequency sweeping with an excitation amplitude of 0.0008 m are shown in Fig. 10b, which exhibit good agreement and validate the electrical dynamics model. In the following sections, the electrostatic force will not be taken into consideration and the Simulink model will be utilized for predicting the electric outputs.

5.2 Comparison of friction models

For triboelectric energy harvesting with sliding mode, friction is an essential factor, which exists at the interface between two distinct materials involving contact and relative sliding. In some publications [22, 23] about sliding-mode triboelectric energy harvesters, the friction is usually modelled by Coulomb's friction law, which depends on two significant parameters, namely the coefficient of static friction μ_s and the coefficient of kinetic friction μ_k . It is well known that the coefficient of static friction is larger than the coefficient of kinetic friction for most materials. According to Coulomb's friction laws, the kinetic friction remains constant during sliding. However, many experimental investigations showed the dependence of kinetic friction on the relative velocity of the rubbing surfaces, where a decreasing

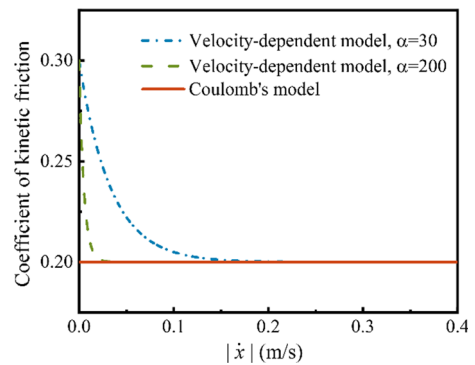


Fig. 11 Friction models

characteristic at values of relative velocity was observed [47]. Therefore, it is worth investigating the difference and effect between Coulomb's model and the velocity-dependent model (exponential-type model).

Figure 11 shows the coefficient of kinetic friction in Coulomb's model and the velocity-dependent model. The difference between the two models is that for the latter, the coefficient of kinetic friction gradually decreases with the relative velocity and tends to be a constant finally. Two different values of the tuning parameter α are used in the velocity-dependent model. It can be seen that a larger tuning parameter results in a sharper decrease in the coefficient of kinetic friction. Larger values of the coefficient of kinetic friction correspond to lower relative

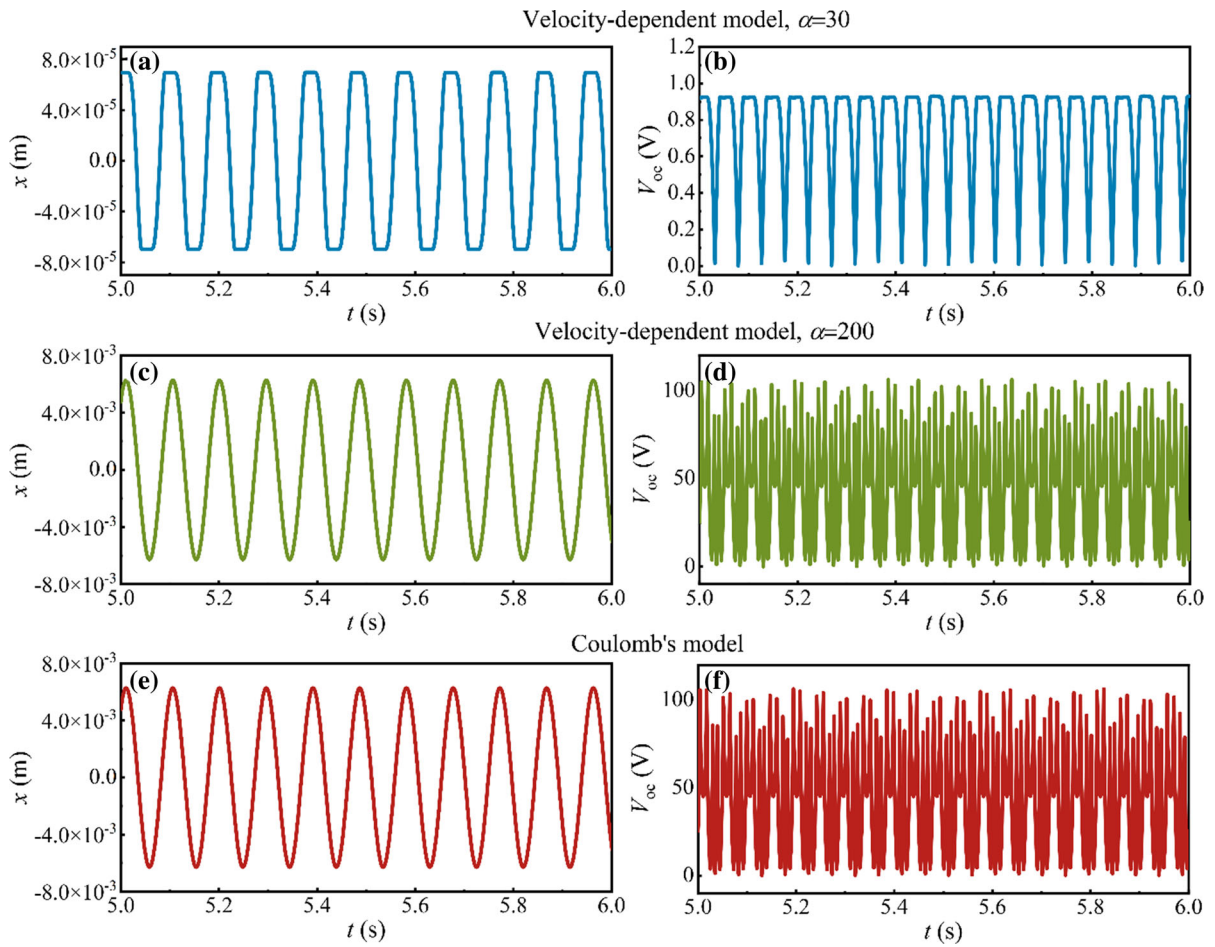


Fig. 12 Structural response and open-circuit voltage under different friction models

velocities with a larger range when α is at a lower level.

To compare the impact of Coulomb’s model and the velocity-dependent model on triboelectric energy harvesting, the friction in the proposed harvester is modelled by using the two types of models, respectively. Meanwhile, the magnets are removed for simplifying the simulation and then comparison. Figure 12 illustrates the relative displacement (left column) of the oscillator and open-circuit voltage (right column) of the sub-harvesters under the velocity-dependent models ($\alpha = 30$ and 200) and Coulomb’s model at $A = 0.0008$ m and $f = 10.5$ Hz. For the velocity-dependent model, when $\alpha = 30$, as shown in Fig. 12a and b, stick–slip vibration with a small amplitude takes place, resulting from a large coefficient of kinetic friction under low velocities, and bringing about a low open-circuit voltage. When a

large value is given to α , the velocity range for large kinetic friction moves to a lower-level region. Consequently, the oscillator vibrates with pure slip motion and a relatively large amplitude, and a high open-circuit voltage is generated, as shown in Fig. 12c and d. For Coulomb’s model, because of its independence of the relative velocity, vibrations with a large amplitude and a high open-circuit voltage are achieved even at fairly low velocities (Fig. 12e and f). It also

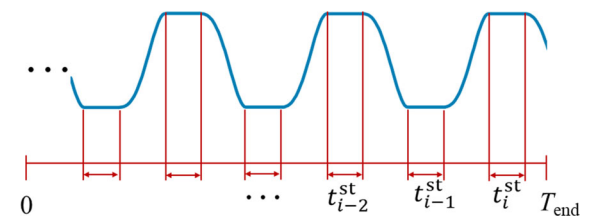


Fig. 13 Sequence of sticks and slips

can be seen that the relative displacements of the oscillator and the open-circuit voltages under the velocity-dependent model when $\alpha = 200$ and Coulomb's model are nearly the same.

The differences between friction models result in distinct sceneries in terms of the stick and slip process. For further investigation, stick duration is studied under the velocity-dependent models and Coulomb's model, since the stick duration is one of the factors of great interest in systems with stick–slip behaviour [48]. Figure 13 shows a sequence of stick and slip, in which the blue line represents the time history of the relative displacement of the oscillator in the proposed harvester. The lasting time of each stick episode is recorded and marked as t_i^{st} , and then, the total stick duration η is expressed as

$$\eta = \frac{\sum t_i^{st}}{T_{end}} \tag{23}$$

in which T_{end} denotes the total time.

Firstly, the stick duration under frequency sweeping with an excitation amplitude of 0.0008 m for the velocity-dependent model with $\alpha = 30$ is illustrated in Fig. 14a. Compared with the frequency response shown in Fig. 7a, it is easier to categorize the motion of the oscillator. When the excitation frequency is relatively low (< 10 Hz), the stick duration is almost 100%, which means the oscillator always sticks with the harvester casing in this region. Stick–slip vibration appears in the frequency range from 10 to 10.8 Hz.

Accordingly, the stick duration drops to a level between 100% and 0. A further increase in the excitation frequency brings about pure slip motion of the oscillator, and the corresponding stick duration is nearly zero. Figure 14b shows a comparison about stick duration among the velocity-dependent models and Coulomb's model. For Coulomb's model, the stick duration falls from 100% to approximate zero at 10 Hz, which means that no stick–slip motion happens in Coulomb's model. The stick duration in the velocity-dependent model with $\alpha = 200$ exhibits the similar scenario compared with that in Coulomb's model. Obviously, there is a big difference between Coulomb's model and the velocity-dependent model with a relatively small tuning parameter ($\alpha = 30$) in light of stick–slip process. For triboelectric energy harvesting systems, the electric performance is strongly linked with the structural dynamics of systems. Particularly for sliding-mode triboelectric energy harvesters, the stick and slip characteristics greatly affect the electric outputs, since there are no charges transferred between the electrodes during stick motion. The difference of the friction models on structural response may directly affect the harvesting efficiency.

A further comparison is made, where the RMS displacement and RMS voltage of the sub-harvesters versus excitation frequency at $A = 0.0008$ m in the velocity-dependent models and Coulomb's model are compared in three cases with different coefficients of kinetic and static friction, namely, case 1 ($\mu_m=0.2$ and

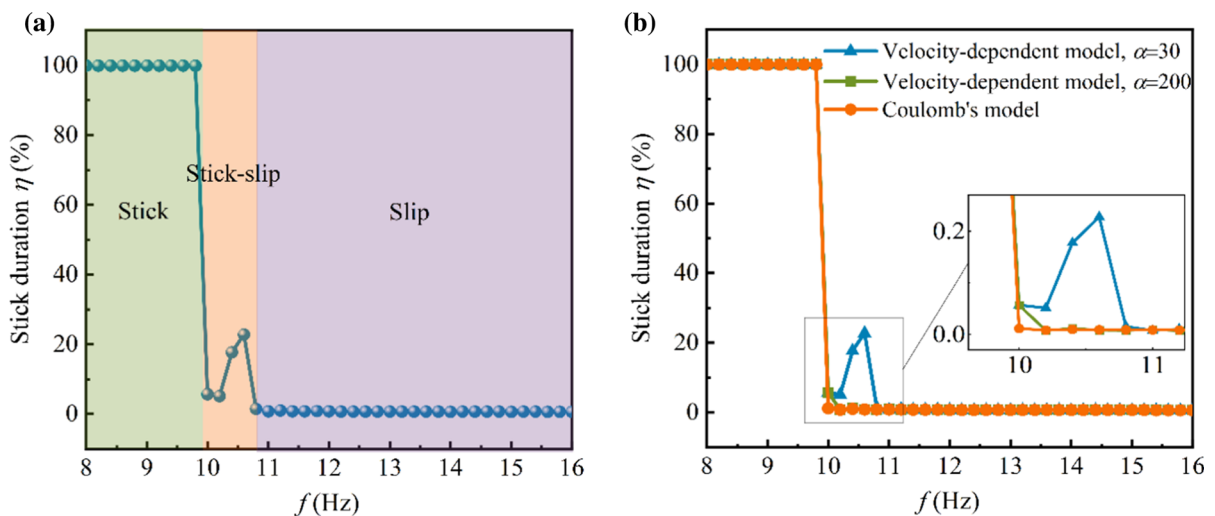
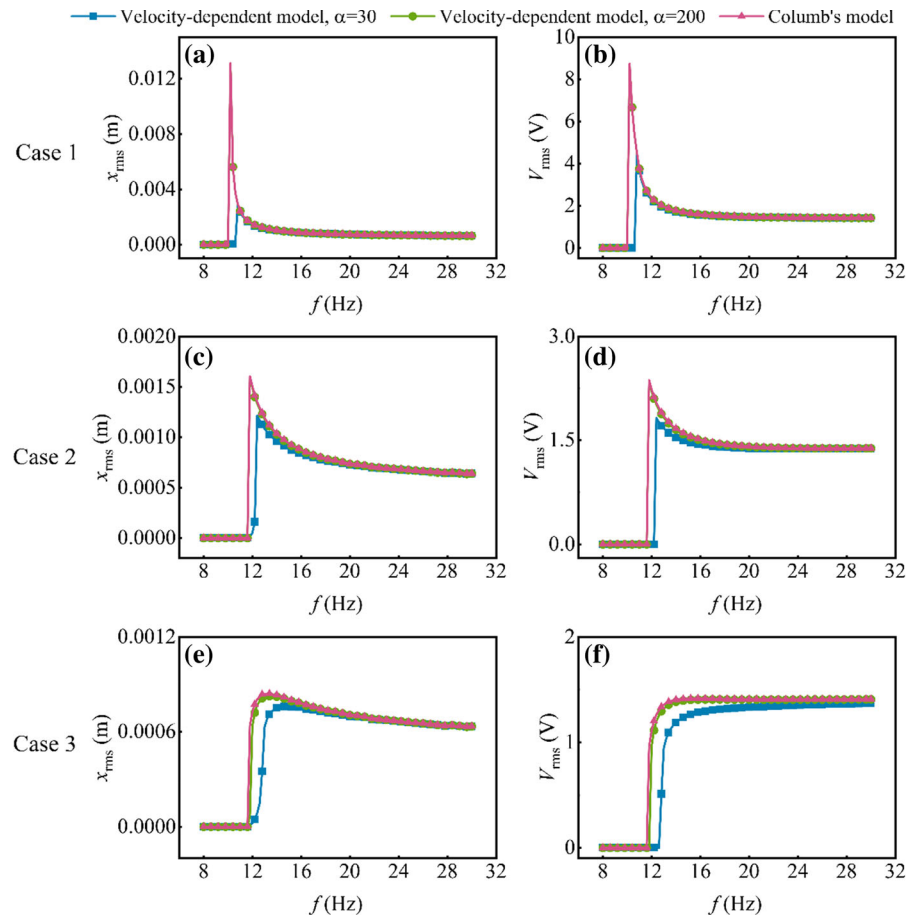


Fig. 14 Stick duration under different friction models

Fig. 15 Frequency response (a) and output voltage (b) under different friction models

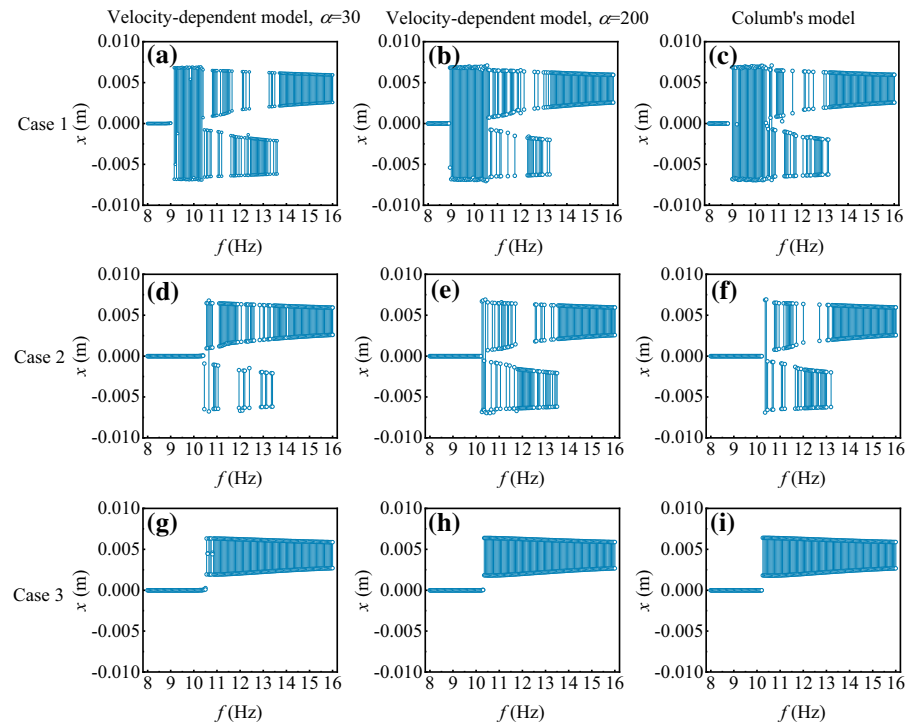


$\mu_s=0.3$), case 2 ($\mu_m=0.2$ and $\mu_s=0.4$) and case 3 ($\mu_m=0.3$ and $\mu_s=0.4$), as shown in Fig. 15. Compared with case 1, a larger coefficient of static friction is used in case 2, and both larger coefficients of static friction and kinetic friction are used in case 3. As observed, in all the three cases, at the peak point, smaller structural response and output voltage are obtained when utilizing the velocity-dependent model with $\alpha = 30$. Particularly in case 1, when both the coefficients of kinetic and static friction are relatively small, fairly big differences exist at the peak point of the vibration amplitude and output voltage versus excitation frequency. However, there are no obvious differences between the velocity-dependent model with $\alpha = 200$ and the Coulomb's model. Actually, by combining Fig. 11, it can be found that when the tuning parameter is relatively small in the velocity-dependent model, large kinetic friction forces act on the oscillator at low velocities, which dissipates kinetic energy like damping [51]. As a consequence, smaller structural

response and output voltage are obtained. Because the coefficient of static friction in case 2 is larger than that in case 1, the frequency range for sticking is larger in case 2, where the vibration amplitude and output voltage also become lower than those in case 1. A much smaller response and output voltage are found when both coefficients of static friction and kinetic friction become larger (in case 3).

For further investigation of the effect of friction on intrawell and interwell dynamics, the frequency response of the bistable harvesting system at $A = 0.001$ m is investigated under the velocity-dependent model and Coulomb's model in the three cases mentioned above, as shown in Fig. 16, where the maximal and minimal vibration amplitudes in steady states at each excitation frequency are marked and connected through vertical lines. The gap between magnet A and magnet B is 10 mm here. As observed, in case 1 (the first row of figures), the frequency bandwidth for interwell oscillation under the velocity-

Fig. 16 Vibration amplitudes of the bistable harvesting system under different friction models



dependent model with $\alpha = 30$ is slightly smaller than that under the velocity-dependent model with $\alpha = 200$ and the Coulomb's model. By comparing case 1 and case 2 (the second row of figures), it can be seen that due to the larger coefficient of static friction in case 2, the frequency range for stick becomes larger than that in case 1. Moreover, the frequency bandwidth for interwell oscillation shrinks dramatically and nearly disappears. In case 3 (the third row of figures), only intrawell oscillation takes place because of both larger coefficients of kinetic and static friction. In case 2 and case 3, the differences in dynamic behaviour between the friction models are almost negligible.

Based on the analysis above, it can be concluded that differences are found between Coulomb's model and the velocity-dependent model. When the friction on the contact interface has an obvious velocity-dependence, the conventional Coulomb's model will not be suitable, which results in an inaccurate prediction of structural response and electric output for the triboelectric energy harvester under this study. Besides, a larger coefficient of static friction brings about a larger frequency bandwidth of stick. The increase in the coefficient of static friction and/or

kinetic friction reduces the frequency bandwidth for interwell oscillation.

5.3 Effect of potential wells

The two pairs of magnets in the proposed harvester create a bistable mechanism, which introduces nonlinearity into the harvesting system. Figure 17 illustrates the potential energy of the harvesting system and the total magnetic force on the oscillator in the parameter region of relative displacement x and magnet gap d . As observed, when the gap is relatively small, the magnetic force exhibits strong nonlinearity. Meanwhile, two valleys and a peak appear in the potential energy. The difference between the valley values and the peak value is called potential barrier. A smaller gap can cause a higher potential barrier. It is well known that a bistable system has two potential wells, resulting in two stable equilibrium points and one unstable equilibrium point, which can lead to two distinct types of steady-state oscillation under a harmonic excitation, namely intrawell oscillation, where the system remains within one of the potential wells centred at one of the stable equilibria, and interwell oscillation, where system trajectory

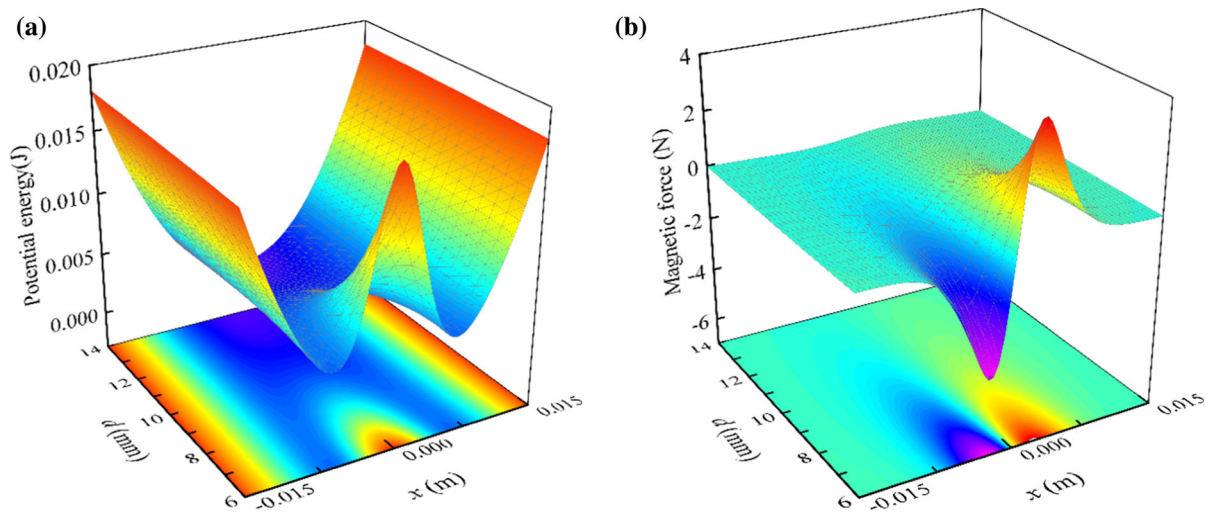
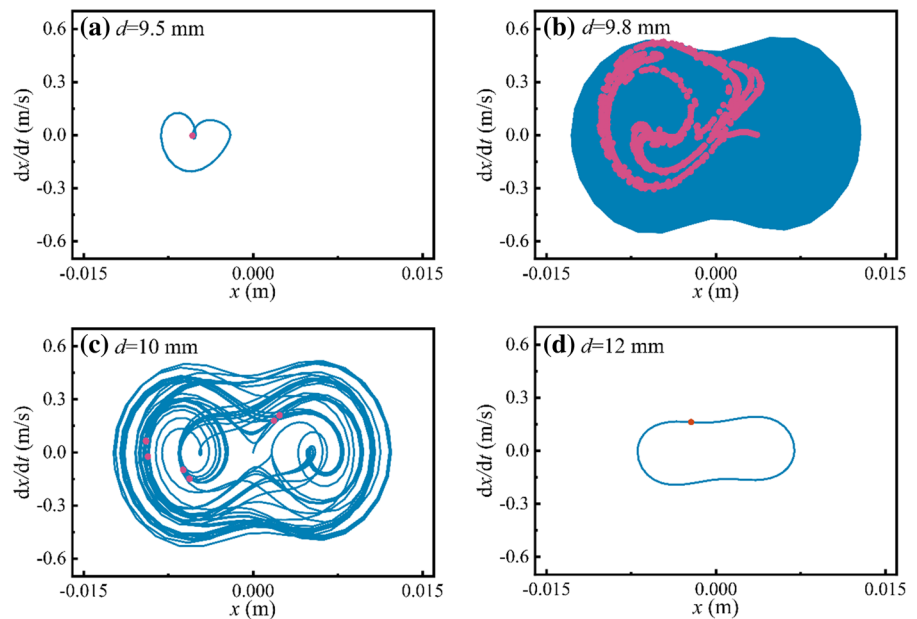


Fig. 17 Potential energy and magnetic force

Fig. 18 Phase portraits and Poincare sections under different magnet gaps at $A = 10$ mm and $f = 5$ Hz

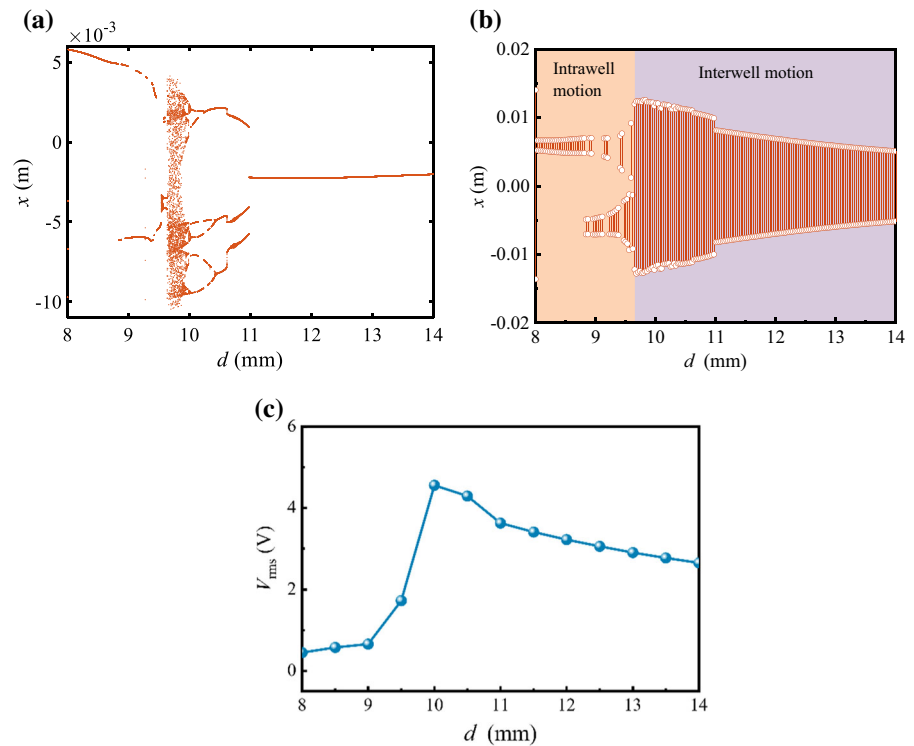


surrounds three equilibria [50]. Single-periodic, multi-periodic, aperiodic, or chaotic motions may take place in both intrawell oscillation and interwell oscillation [51].

The magnet gap directly affects the potential barrier and dynamic behaviours of the harvester, which is an essential parameter in harvester design. Figure 18 shows the phase portraits and Poincare sections under different gaps at $A = 0.010$ m and $f = 5$ Hz. Other parameters utilized in this section are shown in Table 1. When the gap is small (such as $d = 9.5$ mm

in Fig. 18a), single-periodic intrawell oscillation with a small amplitude occurs due to the high potential barrier. A slight increase in the gap brings about a lower potential barrier, consequently causing chaotic interwell oscillation, as shown in Fig. 18b. A further and slight increase in the gap results in multi-periodic interwell oscillation (Fig. 18c). When the gap increases to 12 mm, as shown in Fig. 18d, single-periodic interwell oscillation takes place. Although the oscillator vibrates between the two potential wells, its amplitude is smaller than that when $d = 9.8$ or 10 mm

Fig. 19 Bifurcation diagram of the displacement (a), vibration amplitude (b) and output voltage (c) versus the magnet gap d



due to weaker effect of the bistable mechanism resulting from increase in the gap. It can be seen that a slight variation of the gap can result in distinct responses, which means that the dynamic behaviour of the harvester is sensitive to the magnet gap.

For further investigating the effect of the magnet gap, a bifurcation diagram of the displacement versus the gap at $A = 0.010$ m and $f = 5$ Hz is plotted in Fig. 19a. Besides, the vibration amplitude under gap sweeping is shown in Fig. 19b, in which the maximal and minimal displacement of the oscillator at each gap are connected with vertical lines. By combining the two figures, it is easier to find out the effect of the gap on structural dynamics. When the gap is approximately smaller than 9.6 mm, single-periodic or double-periodic intrawell oscillations take place. A narrow window (from 9.6 to 9.9 mm) is found, in which chaotic interwell oscillation occurs. Multi-periodic interwell oscillation happens in the gap range from 9.9 to 11 mm. When the gap is over 11 mm, only single-periodic interwell oscillation takes place, and the vibration amplitude decreases with the increase in the gap. This reveals that an appropriate gap can bring about large-amplitude vibrations even if the excitation frequency is far away from the natural frequency.

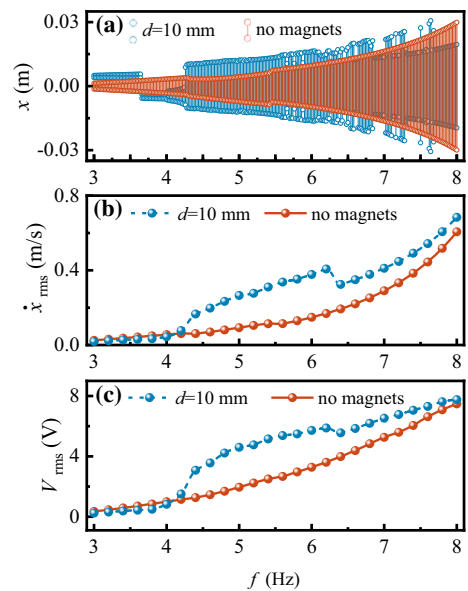


Fig. 20 Comparison of the response (a) RMS velocity (b) and output voltage (c) between the harvesters with and without the bistable mechanism

Figure 19c shows the RMS output voltage versus the magnet gap, which indicates that an optimal gap of

about 10 mm can bring about the highest voltage output under the given excitation.

Actually, it is well known that a bistable mechanism is capable of broadening the frequency bandwidth of energy harvesting systems and enhancing harvesting efficiency. A number of numerical studies about piezoelectric energy harvesters and magnetoelectric energy harvesters revealed that this mechanism could provide much better performance than linear mechanism when the excitation frequency was much less than the natural frequency [52]. Therefore, the enhancement of the bistable mechanism is investigated and verified in the proposed triboelectric energy harvester. As illustrated in Fig. 20a, b and c, the displacement x , RMS velocity \dot{x}_{rms} and the RMS output voltage V_{rms} of the proposed harvester with and without the bistable mechanism under discrete numerical frequency sweeping from 3 to 8 Hz with an amplitude of 0.010 m are compared. As the frequency range is far away from the natural frequency of the harvesting system, the response of the linear harvester (with magnets removed) remains at a relatively low level at low frequencies. However, for the harvester with the bistable mechanism, large-amplitude vibrations and high velocity are obtained when the frequency is over 4.2 Hz. Regarding the electric performance, it can be seen that the output voltage from the harvester with the bistable mechanism is higher than that without the bistable mechanism when the excitation frequency is larger than 4.2 Hz. Particularly in the frequency span from 4.4 to 6.2 Hz, the output voltage from the bistable harvester is approximately twice of that from the linear harvester. When the excitation frequency increases to 8 Hz, the output voltage from the linear harvester nearly catches up with that from the bistable harvester.

Obviously, in the proposed triboelectric energy harvester, the bistable mechanism consisting of the four magnets can bring about large-amplitude and high-velocity responses at off-resonance frequencies, effectively enhance the electric performance at low frequencies.

5.4 Effect of excitation level

In the bistable harvesting system with non-smooth dynamics, the excitation level usually is an essential factor, which not only plays a significant role in the orbit jump from low to high orbits, but also affects the

switch between stick and slip. For investigating the effect of the excitation level, numerical simulations for discrete frequency sweeping in a frequency range from 3 to 8 Hz under different excitation amplitudes are carried out, as shown in Fig. 21. When the excitation amplitude is at a relatively low level (such as $A = 0.002$ m in Fig. 21a), the frequency span for stick makes up over half of the given frequency range. With the increase in frequency, the intrawell oscillation and interwell oscillation occur successively. When the system is exposed to an excitation with a higher amplitude (such as $A = 0.006$ m in Fig. 21b), the bandwidth for intrawell oscillation becomes wider and the span for stick in the given frequency region shrinks accordingly. A further increase in the excitation amplitude (such as $A = 0.010$ m in Fig. 21c) results in the disappearance of stick in the given frequency range. These results indicate that the harvester requires a relatively large excitation amplitude to avoid pure stick and ensure a considerable electric output since no electricity is generated during stick motion.

Under different excitation levels, the bistable system may need different magnet gaps for the best electric performance. Figure 22a shows the RMS output voltage in the parameter region of magnet gap and excitation amplitude at $f = 5$ Hz. As observed, when the excitation amplitude varies from 0.005 to 0.010 m, the optimal gap changes slightly, nearly constant in the interval between 9.5 and 10.5 mm, which means that the excitation amplitude does not have a great effect on the optimal gap in the amplitude range. In Fig. 22b, the RMS output voltage is illustrated in the parameter region of magnet gap and excitation frequency at $A = 0.010$ m. It can be seen that the optimal gap is obviously influenced by the excitation frequency, which decreases with the increase in the excitation frequency. This indicates that the harvester requires a smaller gap between the magnets when exposed to an excitation with a higher frequency.

5.5 Grating segmentation of films

In this work, grating-patterned films are introduced in the harvester design, which is different from most sliding-mode harvesters with single-unit films. According to the electric model of the harvester established in Sect. 4, the equivalent capacitance and

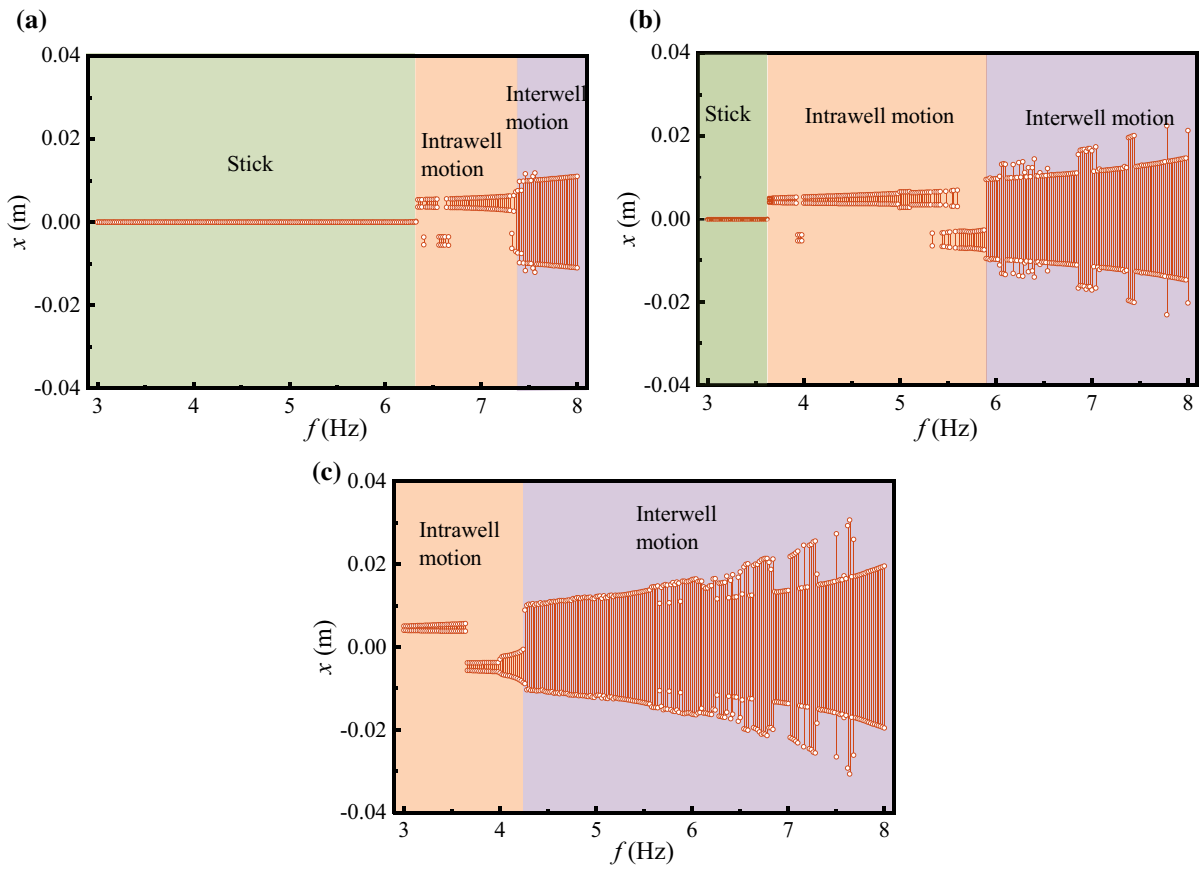


Fig. 21 Frequency responses under different excitation amplitudes: **a** $A = 0.002$ m; **b** $A = 0.006$ m; **c** $A = 0.010$ m

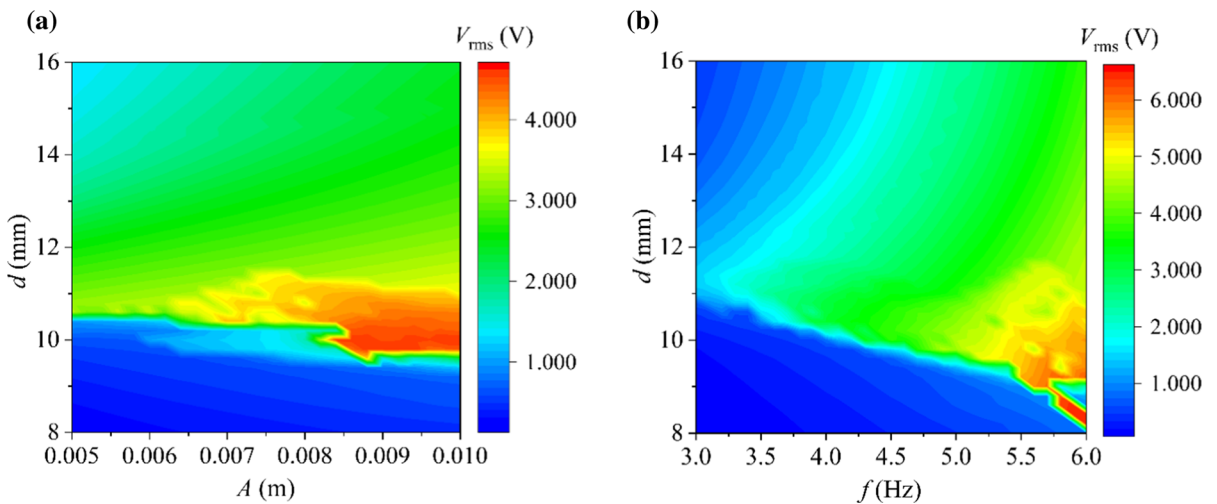


Fig. 22 RMS Output voltage **(a)** in the parameter region of gap d and excitation amplitude A at $f = 5$ Hz, and **(b)** in the parameter region of gap d and excitation frequency f at $A = 0.010$ m

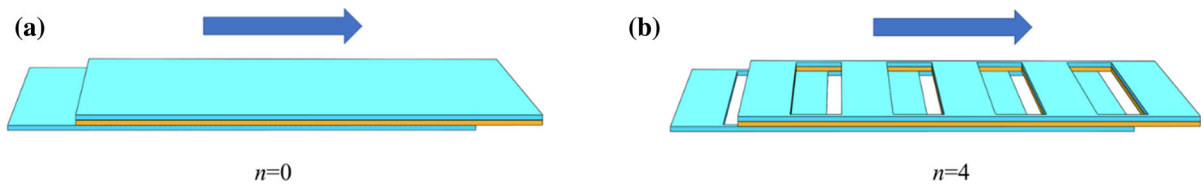


Fig. 23 Two different segmentation patterns for films

open-circuit voltage are functions of the overlapping area between the two electrodes, which depends on both the relative displacement and the shape of the films. Under the same structural response, the films with different grating patterns may have distinct electrical dynamics. For the films in the proposed harvester, the number of the hollowed-out units n is a crucial parameter, determining the grating segmentation of the films.

Two different segmentation patterns ($n = 0$ and $n = 4$) for the films are compared to explore the difference in the process of power generation, as shown in Fig. 23a and b, where the top electrodes (films) slide from left to right at a constant speed while the bottom electrodes (films) are fixed. Herein, a speed of 0.03 m/s is utilized. In the initial position, the top electrodes fully overlap with the bottom electrodes. To avoid the singularity when the top electrodes completely slide out of the bottom electrodes, the sliding distance is set to $0.9L$ (L is the length of the electrodes). Figure 24a and b illustrates the overlapping area and the open-circuit voltage during motion of the top electrodes from the left to right. It can be seen that for the single-unit films ($n = 0$), the overlapping area decreases linearly and the open-circuit voltage increases slightly when the moving

distance is relatively small. Only when the top electrode is close to the right end of the bottom electrode, the open-circuit voltage can increase to a relatively high level. This means during vibration, the single-unit films require large amplitudes to achieve high electric outputs, while for $n = 4$, the overlapping area experiences several peaks during motion. Although the total area of the grating-patterned films ($n = 4$) is smaller than that of the single-unit films ($n = 0$), the open-circuit voltage generated by the former is much higher than that generated by the latter. Even when the sliding distance is small, the grating-patterned films can also achieve higher open-circuit voltage than the single-unit films, which reveals the superiority of the grating-structured films.

A further comparison among the films with different grating patterns in the proposed harvester under an excitation with an amplitude of 0.010 m and a frequency of 5 Hz is shown in Fig. 25, where 5 different segmentation patterns ($n = 0, 1, 2, 3$ and 4) are involved. The magnet gap is set to 10 mm, and the other parameters utilized here are shown in Table 1. According to Sect. 5.3, interwell motion takes place under the given conditions. The figures in the first and second rows in Fig. 25 illustrate the overlapping area A_1 and open-circuit voltage V_{oc} , and the figures in the

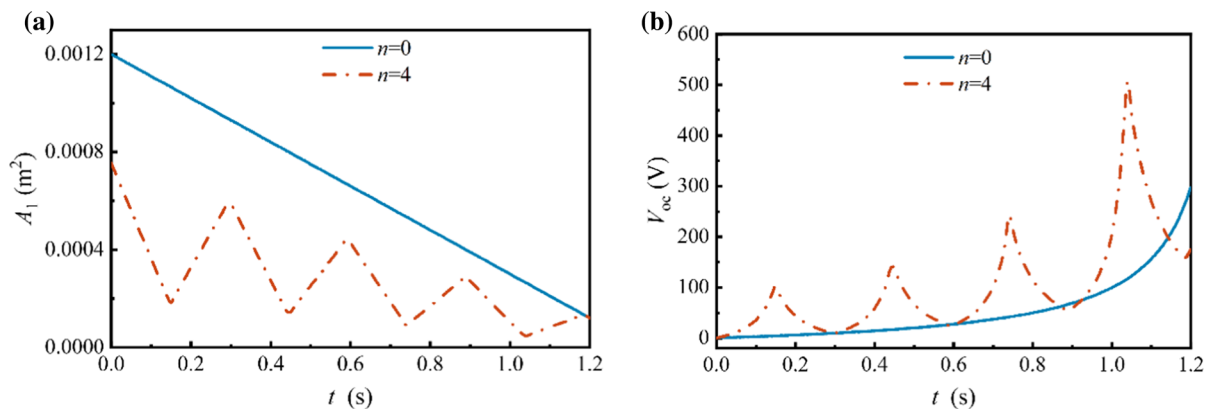


Fig. 24 Overlapping area (a) and open-circuit voltage (b) for two different segmentation patterns of films

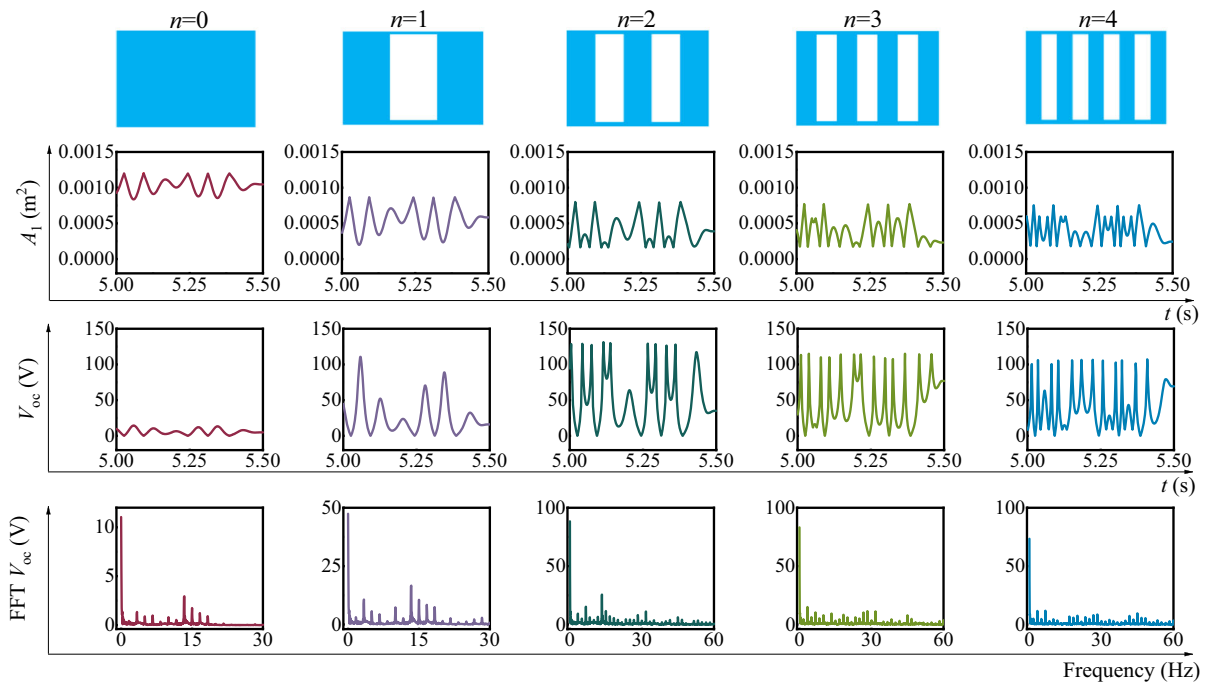


Fig. 25 Comparison of the films with different grating patterns

third row show the fast Fourier transform (FFT) for the open-circuit voltage. As observed, the overlapping area of the single-unit films ($n = 0$) varies in a small range (between 8.4×10^{-4} and 11.9×10^{-4} m²) during vibration, resulting in a small open-circuit voltage with a peak value less than 5 V. When $n = 1$, due to the change in the segmentation structure, the variation range of the overlapping area becomes wider (between 2.0×10^{-4} and 8.6×10^{-4} m²).

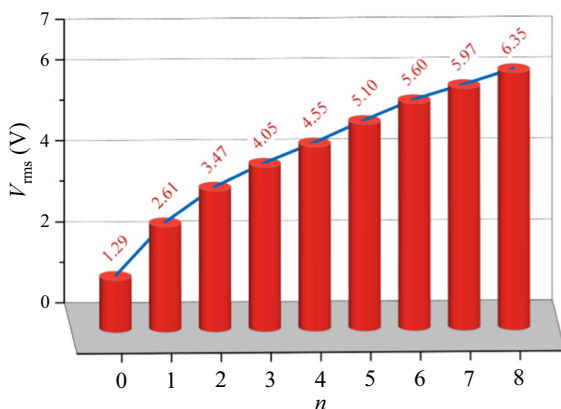


Fig. 26 Output voltage versus the number of hollowed-out units

Consequently, a much higher open-circuit voltage with a peak value of 109.4 V is obtained. Moreover, according to the FFT results, it is found that the grating-patterned films ($n = 1$) can generate higher-frequency components in the open-circuit voltage compared with the single-unit films ($n = 0$). This characteristic becomes more obvious when $n = 2, 3$ and 4. More high-frequency components in the open-circuit voltage are induced when increasing the number of hollowed-out units n . The analysis above indicates that compared with the single-unit films, the grating-patterned films can effectively enhance the rangeability of overlapping area between electrodes, which accordingly improves the open-circuit voltage and brings about high-frequency components in the open-circuit voltage in the meantime. Therefore, it is reasonable to believe that the output performance of the harvester can be enhanced through appropriately increasing the number of hollowed-out unit on the films.

Figure 26 illustrates the RMS output voltage V_{rms} versus the number of hollowed-out units n at $A = 0.010$ m and $f = 5$ Hz with the magnet gap of 10 mm. As observed, the output voltage increases with the increase in the number of the hollowed-out units.

And the output voltage from the grating-patterned films with 8 hollowed-out units ($n = 8$) is nearly five times as high as that from the single-unit films ($n = 0$). It can be concluded that the grating-patterned films can effectively improve the electric output performance of the proposed harvester via increasing the number of the hollowed-out units on the films. It should be noticed that the approximate analytical relationship between the output voltage, transferred charges and relative displacement established in Sect. 4 is based on the condition that the width of the units is much larger than the thickness of the films so that the edge effect can be neglected. In this work, the number of the hollowed-out units is investigated in a relatively small range which satisfies the condition. When the number of the hollowed-out units reaches a fairly large value, the width of the units becomes comparable with the thickness of the films. In that case, the non-ideal edge effect is significant and cannot be ignored any longer [2].

5.6 Overall electric performance

The proposed harvester consists of two sub-harvesters, whose electric outputs are studied extensively in an independent circuit (as shown in Fig. 10a). However, in practice, it is usually required that the sub-harvesters work in a single circuit. Therefore, it is worth investigating the overall electric performance of the harvester. Figure 27 shows a rectifying circuit established in Simulink which can be utilized in practical applications for the harvester. The two sub-harvesters are wired with two rectifiers, which convert the alternating current (AC) to direct current (DC). A smoothing capacitor ($1 \mu\text{F}$) is employed to smooth the AC and make the current (or voltage) steady. For assessing the electric performance, a load resistor R is connected with the output port of the circuit. The excitation amplitude and frequency are 0.002 m and 8 Hz. The magnet gap is 10 mm. Interwell motion takes place under the given conditions according to Fig. 21a. Other parameters utilized here are shown in Table.1.

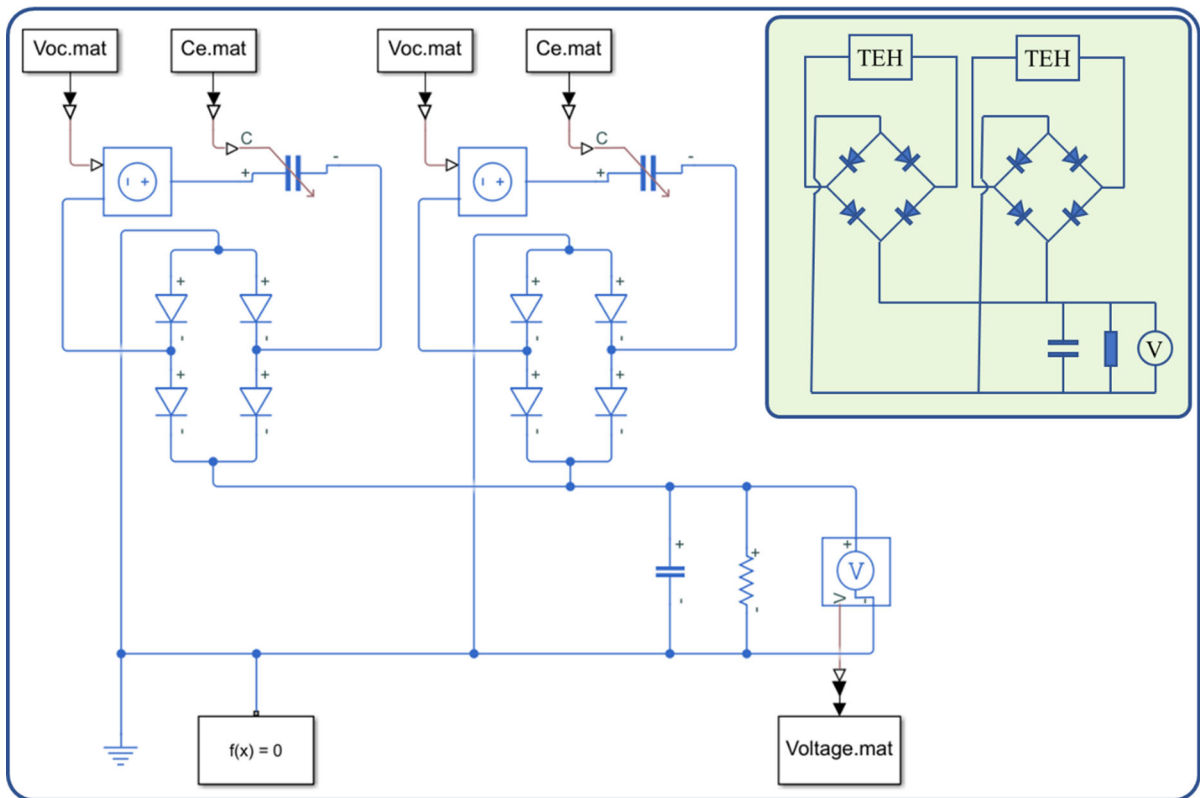


Fig. 27 Rectifying circuit for the harvester

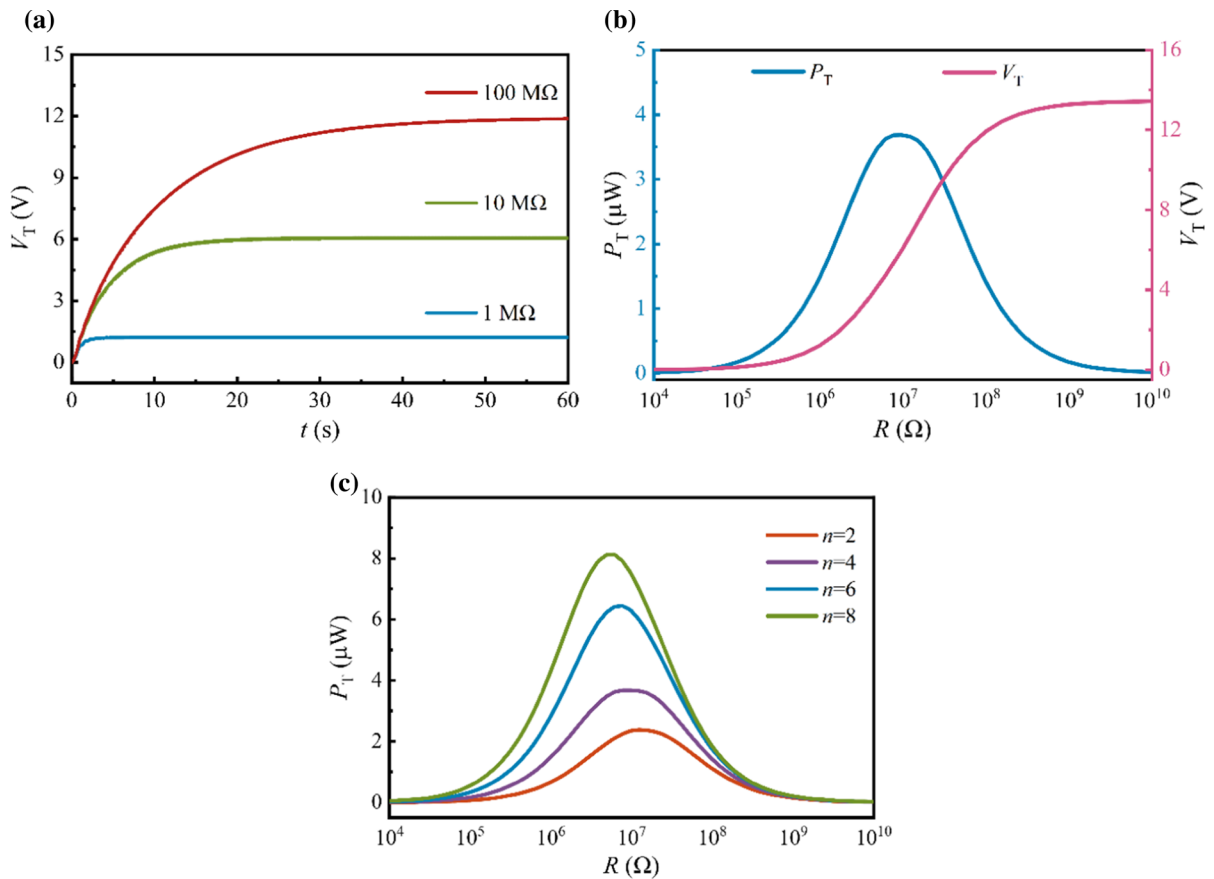


Fig. 28 Overall electric performance: **a** Time history of the total output voltage; **b** the total output voltage and total power versus the load resistor; **c** the total power under different numbers of hollowed-out units

Figure 28a shows the time history of the total output voltage V_T across the load resistor R . The total voltage reaches a constant value in a few seconds, which increases from 1.2 to 11.9 V when R increases from 1 MΩ to 100 MΩ. However, this does not mean the total output power exhibits the similar tendency. Only when the load impedance is compatible with the internal impedance of the harvester, the best performance can be achieved. An optimal resistance exists for the harvester for the highest output power. Figure 28b illustrates the total output voltage V_T and total power P_T in the steady state under different load resistance, from which it can be seen that the highest power appears at $R = 10$ MΩ approximately. The total power P_T versus the load resistance under different numbers of the hollowed-out units is shown in Fig. 28c, which indicates that the increase in the number of hollowed-out units can result in a slight decrease in the optimal resistance. The reason is that

the total area of the films decreases with the increase in the number of hollowed-out units, causing the decrease in inherent capacitance of the harvester. Note that the internal impedance mainly comes from the inherent capacitance [2].

6 Conclusions

In this paper, a novel design of a triboelectric energy harvester is developed for scavenging vibration energy, in which an oscillator can slide inside a casing. Consequently, electricity can be generated by sliding mode. The contact surfaces between the oscillator and the casing are attached with grating-patterned films. A bistable mechanism in the form of two pairs of magnets is employed for broadening frequency bandwidth. The modelling of the structural dynamics and electrical dynamics is presented, and

detailed numerical simulations are carried out. This paper is the first study of the nonlinear structural vibration of a triboelectric energy harvester with grating-patterned films. It also presents the first triboelectric energy harvester combining the grating-patterned films and the bistable mechanism for dual enhancement of harvesting efficiency. The main conclusions are drawn as follows:

- (1) The effect of the electrostatic force on structural dynamics can be ignored reasonably when the surface charge density is low. A high surface charge density brings about a non-negligible reduction on vibration amplitude. A Simulink model is established for predicting the electric output, which exhibits good agreement with the theoretical model (coupled model).
- (2) An inaccurate prediction of structural response and electric output for the triboelectric energy harvester can be made with the conventional Coulomb's model when the friction on the contact interface has an obvious velocity dependence. The frequency range for stick increases with the increase in coefficient of static friction. In contrast, the frequency bandwidth for interwell oscillation decreases with the increase in coefficient of static friction and/or kinetic friction.
- (3) The bistable mechanism is found to broaden the frequency bandwidth of the harvester, resulting in a larger amplitude and a higher relative velocity when the excitation frequency is lower than its natural frequency, which accordingly brings about a higher output voltage.
- (4) The excitation level plays a significant role in the bistable and non-smooth harvesting system. Low excitation levels cause stick, which also will not enable the oscillator to overcome the potential barriers, resulting in intrawell motion. A smaller gap between the magnets is required for the highest power output when the excitation level is higher.
- (5) The segmentation structure of the films directly affects the electrical dynamics of the harvester. The power output efficiency can be effectively enhanced by increasing the number of the hollowed-out units on the films to a certain limit.
- (6) The overall electric performance of the harvester is investigated in a rectifying circuit built in Simulink. The optimal resistance is found to match the internal impedance of the harvester for the highest output power, which slightly decreases with the increase in the number of the hollowed-out units.

Acknowledgements The first author is sponsored by a University of Liverpool and China Scholarship Council joint scholarship.

Authors' contributions Both authors contributed to the conception, methodology, analysis of the results and writing of all the versions of the paper. HZ performed derivation of equations, computer programming and numerical analysis. HO supervised the research work.

Funding There is not a funding specific for this research work.

Data availability The authors have the data and materials that support the work reported in this paper. They can be provided upon request. The datasets generated during and/or analysed during the current study are available from the corresponding author on reasonable request.

Code availability The computer code used in generating the numerical results in this paper can be disclosed upon reasonable request and agreement of a proper acknowledgment of the code.

Declarations

Conflict of interest The authors declare no conflict of interest in this work.

Consent to participate Both authors gave consent to participate in the research work and the writing of this paper.

Consent for publication Both authors would like to submit this paper to *Nonlinear Dynamics* for publication.

Open Access This article is licensed under a Creative Commons Attribution 4.0 International License, which permits use, sharing, adaptation, distribution and reproduction in any medium or format, as long as you give appropriate credit to the original author(s) and the source, provide a link to the Creative Commons licence, and indicate if changes were made. The images or other third party material in this article are included in the article's Creative Commons licence, unless indicated

otherwise in a credit line to the material. If material is not included in the article's Creative Commons licence and your intended use is not permitted by statutory regulation or exceeds the permitted use, you will need to obtain permission directly from the copyright holder. To view a copy of this licence, visit <http://creativecommons.org/licenses/by/4.0/>.

Appendix A

The harvesting system in this work is a non-smooth system. The transition time instants at switch between stick and slip are captured. The flowchart for solving the non-smooth system is shown below. see Fig. 29.

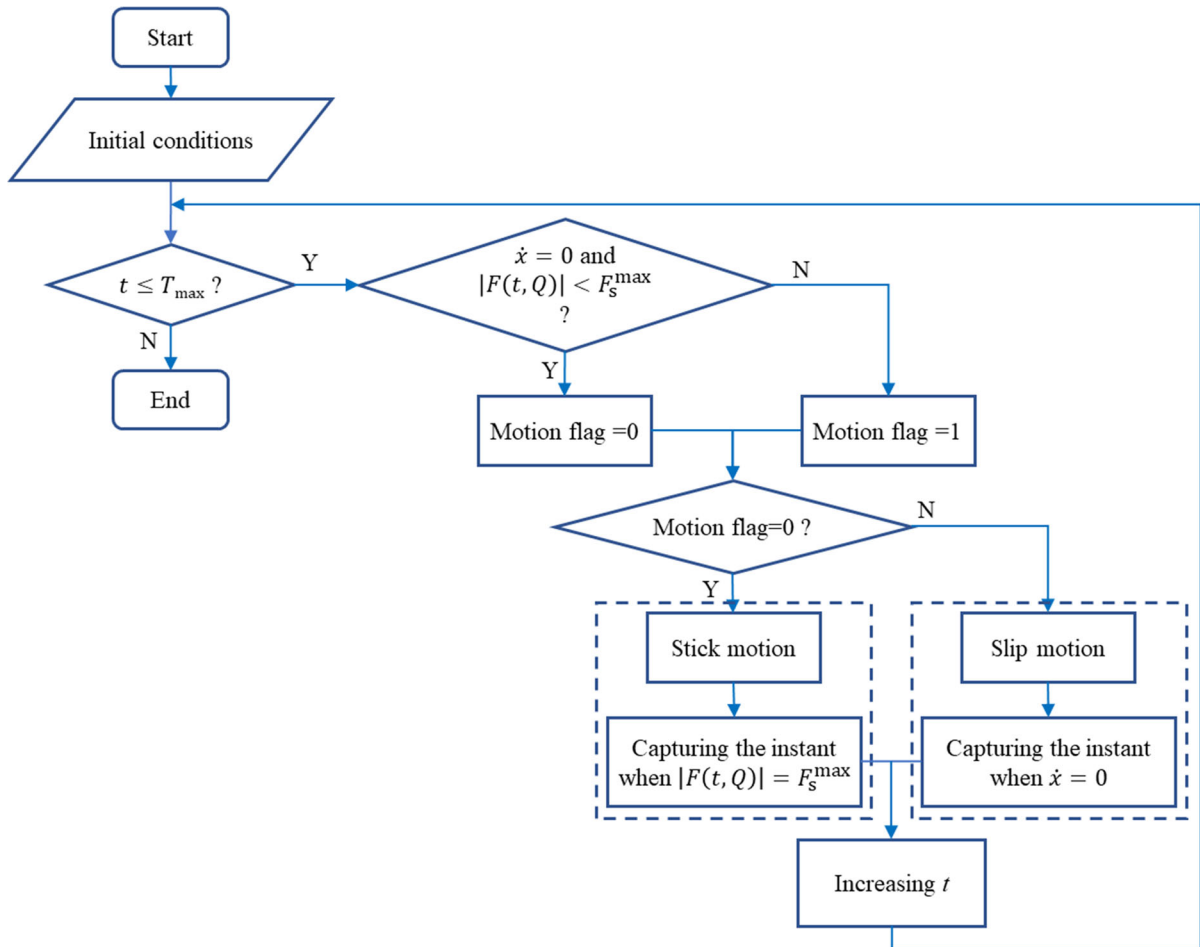


Fig. 29 Flowchart for numerical simulations

References

- Fan, F.R., Tian, Z.Q., Wang, Z.L.: Flexible triboelectric generator. *Nano Energy* **1**, 328–334 (2012). <https://doi.org/10.1016/j.nanoen.2012.01.004>
- Zhang, C., Wang, Z.L.: *Triboelectric nanogenerators*. Springer, Cham (2016)
- Rahman, M.T., Rana, S.S., Salauddin, M., Maharjan, P., Bhatta, T., Park, J.Y.: Biomechanical energy-driven hybridized generator as a universal portable power source for smart/wearable electronics. *Adv. Energy Mater.* **1903663**, 1–14 (2020). <https://doi.org/10.1002/aenm.201903663>
- Yang, Z., Yang, Y., Liu, F., Wang, Z., Li, Y., Qiu, J., Xiao, X., Li, Z., Lu, Y., Ji, L., Wang, Z.L., Cheng, J.: Power backpack for energy harvesting and reduced load impact. *ACS Nano* **15**, 2611–2623 (2021). <https://doi.org/10.1021/acsnano.0c07498>
- Wang, Y., Yang, E., Chen, T., Wang, J., Hu, Z., Mi, J., Pan, X., Xu, M.: A novel humidity resisting and wind direction adapting flag-type triboelectric nanogenerator for wind energy harvesting and speed sensing. *Nano Energy* **78**, 105279 (2020). <https://doi.org/10.1016/j.nanoen.2020.105279>
- Zhang, L., Meng, B., Xia, Y., Deng, Z., Dai, H., Hagedorn, P., Peng, Z., Wang, L.: Galloping triboelectric nanogenerator for energy harvesting under low wind speed. *Nano Energy* **70**, 104477 (2020). <https://doi.org/10.1016/j.nanoen.2020.104477>
- Ravichandran, A.N., Calmes, C., Serres, J.R., Ramuz, M., Blayac, S.: Compact and high performance wind actuated venturi triboelectric energy harvester. *Nano Energy* **62**, 449–457 (2019). <https://doi.org/10.1016/j.nanoen.2019.05.053>
- Paosangthong, W., Torah, R., Beeby, S.: Recent progress on textile-based triboelectric nanogenerators. *Nano Energy* **55**, 401–423 (2019). <https://doi.org/10.1016/j.nanoen.2018.10.036>
- Han, X., Jiang, D., Qu, X., Bai, Y., Cao, Y., Luo, R., Li, Z.: A stretchable, self-healable triboelectric nanogenerator as electronic skin for energy harvesting and tactile sensing. *Materials (Basel)* **14**, 1–10 (2021). <https://doi.org/10.3390/ma14071689>
- Real, F., Batou, A., Ritto, T., Desceliers, C.: Stochastic modeling for hysteretic bit–rock interaction of a drill string under torsional vibrations. *J. Vib. Control.* (2019). <https://doi.org/10.1177/ToBeAssigned>
- Hossain, N.A., Yamomo, G.G., Willing, R., Towfighian, S.: Effect of dielectric material and package stiffness on the power generation in a packaged triboelectric energy harvesting system for total knee replacement. *J. Biomech. Eng.* (2021). <https://doi.org/10.1115/1.4051220>
- Pang, Y.K., Li, X.H., Chen, M.X., Han, C.B., Zhang, C., Wang, Z.L.: Triboelectric nanogenerators as a self-powered 3d acceleration sensor. *ACS Appl. Mater. Interfaces* **7**, 19076–19082 (2015). <https://doi.org/10.1021/acsmi.5b04516>
- Kwon, D.S., Pyo, S., Kim, J.: Self-powered wind sensor based on triboelectric generator with curved flap array for multi-directional wind speed detection. *Proc. IEEE Int. Conf. Micro Electro Mech. Syst.* **190**, 542–545 (2020). <https://doi.org/10.1109/MEMS46641.2020.9056275>
- Adly, M.A., Arafa, M.H., Hegazi, H.A.: Modeling and optimization of an inertial triboelectric motion sensor. *Nano Energy* **85**, 105952 (2021). <https://doi.org/10.1016/j.nanoen.2021.105952>
- Chen, M., Wang, Z., Zheng, Y., Zhang, Q., He, B., Yang, J., Qi, M., Wei, L.: Flexible tactile sensor based on patterned Ag-nanofiber electrodes through electrospinning. *Sensors* **21**, 1–11 (2021). <https://doi.org/10.3390/s21072413>
- Xi, Y., Hua, J., Shi, Y.: Noncontact triboelectric nanogenerator for human motion monitoring and energy harvesting. *Nano Energy* **69**, 104390 (2020). <https://doi.org/10.1016/j.nanoen.2019.104390>
- Lan, L., Xiong, J., Gao, D., Li, Y., Chen, J., Lv, J., Ping, J., Ying, Y., Lee, P.S.: Breathable nanogenerators for an on-plant self-powered sustainable agriculture system. *ACS Nano* **15**, 5307–5315 (2021). <https://doi.org/10.1021/acsnano.0c10817>
- Nelson, D., Ibrahim, A., Towfighian, S.: A tunable triboelectric wideband energy harvester. *J. Intell. Mater. Syst. Struct.* **30**, 1745–1756 (2019). <https://doi.org/10.1177/1045389X19844012>
- Fu, Y., Ouyang, H., Davis, R.B.: Nonlinear dynamics and triboelectric energy harvesting from a three-degree-of-freedom vibro-impact oscillator. *Nonlinear Dyn.* **92**, 1985–2004 (2018). <https://doi.org/10.1007/s11071-018-4176-3>
- Fu, Y., Ouyang, H., Davis, R.B.: Triboelectric energy harvesting from the vibro-impact of three cantilevered beams. *Mech. Syst. Signal Process.* **121**, 509–531 (2019). <https://doi.org/10.1016/j.ymsp.2018.11.043>
- Wang, K., Zhou, J., Ouyang, H., Chang, Y., Xu, D.: A dual quasi-zero-stiffness sliding-mode triboelectric nanogenerator for harvesting ultralow-low frequency vibration energy. *Mech. Syst. Signal Process.* **151**, 107368 (2021). <https://doi.org/10.1016/j.ymsp.2020.107368>
- Fu, Y., Ouyang, H., Benjamin Davis, R.: Nonlinear structural dynamics of a new sliding-mode triboelectric energy harvester with multistability. *Nonlinear Dyn.* **6**, 1–22 (2020). <https://doi.org/10.1007/s11071-020-05645-z>
- Fu, Y., Ouyang, H., Davis, R.B.: Effects of electrical properties on vibrations via electromechanical coupling in triboelectric energy harvesting. *J. Phys. D: Appl. Phys.* **53**, 1–24 (2020)
- Singh, H.H., Khare, N.: Improved performance of ferroelectric nanocomposite flexible film based triboelectric nanogenerator by controlling surface morphology, polarizability, and hydrophobicity. *Energy* **178**, 765–771 (2019). <https://doi.org/10.1016/j.energy.2019.04.150>
- Bhatta, T., Maharjan, P., Cho, H., Park, C., Yoon, S.H., Sharma, S., Salauddin, M., Rahman, M.T., Rana, S.S., Park, J.Y.: High-performance triboelectric nanogenerator based on MXene functionalized polyvinylidene fluoride composite nanofibers. *Nano Energy* **81**, 105670 (2021). <https://doi.org/10.1016/j.nanoen.2020.105670>
- Mutlu, S., Unlu, K., Gevrek, T.N., Sanyal, A.: Expanding the versatility of poly(dimethylsiloxane) through polymeric modification: An effective approach for improving triboelectric energy harvesting performance. *Smart Mater.*

- Struct. **29**, 035024 (2020). <https://doi.org/10.1088/1361-665X/ab6ba6>
27. Nafari, A., Sodano, H.A.: Surface morphology effects in a vibration based triboelectric energy harvester. *Smart Mater. Struct.* **27**, 015029 (2018). <https://doi.org/10.1088/1361-665X/aa9ccb>
 28. Fan, F., Lin, L., Zhu, G., Wu, W., Zhang, R., Wang, Z.L.: Transparent triboelectric nanogenerators and self-powered pressure sensors based on micropatterned plastic films. *Nano Lett.* **12**, 3109–3114 (2012). <https://doi.org/10.1021/nl300988z>
 29. Dhakar, L., Tay, F.E.H., Lee, C.: Development of a broadband triboelectric energy harvester with SU-8 micropillars. *J. Microelectromech. Syst.* **24**, 91–99 (2015). <https://doi.org/10.1109/JMEMS.2014.2317718>
 30. Zhai, C., Chou, X., He, J., Song, L., Zhang, Z., Wen, T., Tian, Z., Chen, X., Zhang, W., Niu, Z., Xue, C.: An electrostatic discharge based needle-to-needle booster for dramatic performance enhancement of triboelectric nanogenerators. *Appl. Energy*. **231**, 1346–1353 (2018). <https://doi.org/10.1016/j.apenergy.2018.09.120>
 31. Lin, Z., Chen, J., Yang, J.: Recent progress in triboelectric nanogenerators as a renewable and sustainable power source. *J. Nanomater.* **2016**, 1–24 (2016). <https://doi.org/10.1155/2016/5651613>
 32. Zou, H.X., Li, M., Zhao, L.C., Gao, Q.H., Wei, K.X., Zuo, L., Qian, F., Zhang, W.M.: A magnetically coupled bistable piezoelectric harvester for underwater energy harvesting. *Energy* **217**, 119429 (2021). <https://doi.org/10.1016/j.energy.2020.119429>
 33. Costa, L.G., Monteiro, L.L., Pacheco, P.M.C.L., Savi, M.A.: A parametric analysis of the nonlinear dynamics of bistable vibration-based piezoelectric energy harvesters. *J. Intell. Mater. Syst. Struct.* **32**, 699–723 (2021). <https://doi.org/10.1177/1045389X20963188>
 34. Yu, N., Ma, H., Wu, C., Yu, G., Yan, B.: Modeling and experimental investigation of a novel bistable two-degree-of-freedom electromagnetic energy harvester. *Mech. Syst. Signal Process.* **156**, 107608 (2021). <https://doi.org/10.1016/j.ymssp.2021.107608>
 35. Wang, L., Chen, R., Ren, L., Xia, H., Zhang, Y.: Design and experimental study of a bistable magnetolectric vibration energy harvester with nonlinear magnetic force scavenging structure. *Int. J. Appl. Electromagn. Mech.* **60**, 489–502 (2019). <https://doi.org/10.3233/JAE-180074>
 36. Deng, H., Ye, J., Du, Y., Zhang, J., Ma, M., Zhong, X.: Bistable broadband hybrid generator for ultralow-frequency rectilinear motion. *Nano Energy* **65**, 1–9 (2019). <https://doi.org/10.1016/j.nanoen.2019.103973>
 37. Micro-actuator, B.: Toward self-control systems for neurogenic underactive bladder: a triboelectric nanogenerator sensor integrated with a bistable micro-actuator. *ACS Nano* **12**, 3487–3501 (2018). <https://doi.org/10.1021/acsnano.8b00303>
 38. Berger, E.J.: Friction modeling for dynamic system simulation. *Appl. Mech. Rev.* **55**, 535–577 (2002). <https://doi.org/10.1115/1.1501080>
 39. Won, H.I., Chung, J.: Stick–slip vibration of an oscillator with damping. *Nonlinear Dyn.* **86**, 257–267 (2016). <https://doi.org/10.1007/s11071-016-2887-x>
 40. Cho, J.Y., Jeong, S., Jabbar, H., Song, Y., Ahn, J.H., Kim, J.H., Jung, H.J., Yoo, H.H., Sung, T.H.: Piezoelectric energy harvesting system with magnetic pendulum movement for self-powered safety sensor of trains. *Sensors Actuators, A Phys.* **250**, 210–218 (2016). <https://doi.org/10.1016/j.sna.2016.09.034>
 41. Yung, K.W., Landecker, P.B., Villani, D.D.: An analytic solution for the force between two magnetic dipoles. *Magn. Electr. Sep.* **9**, 39–52 (1998). <https://doi.org/10.1155/1998/79537>
 42. Niu, S., Zhou, Y.S., Wang, S., Liu, Y., Lin, L., Bando, Y., Wang, Z.L.: Simulation method for optimizing the performance of an integrated triboelectric nanogenerator energy harvesting system. *Nano Energy* **8**, 150–156 (2014). <https://doi.org/10.1016/j.nanoen.2014.05.018>
 43. Niu, S., Wang, Z.L.: Theoretical systems of triboelectric nanogenerators. *Nano Energy* **14**, 161–192 (2014). <https://doi.org/10.1016/j.nanoen.2014.11.034>
 44. Tao, K., Lye, S.W., Miao, J., Tang, L., Hu, X.: Out-of-plane electret-based MEMS energy harvester with the combined nonlinear effect from electrostatic force and a mechanical elastic stopper. *J. Micromechanics Microengineering.* **25**, 104014 (2015). <https://doi.org/10.1088/0960-1317/25/10/104014>
 45. Boisseau, S., Despesse, G., Ahmed, B.: Electrostatic conversion for vibration energy harvesting. *Small-Scale Energy Harvest.* **96**, 1–39 (2012). <https://doi.org/10.5772/51360>
 46. Zhao, H., Ouyang, H.: Erratum: theoretical investigation and experiment of a disc-shaped triboelectric energy harvester with a magnetic bistable mechanism. *Smart Mater. Struct.* **30**, 119501 (2021). <https://doi.org/10.1088/1361-665X/ac26a7>
 47. Popp, K., Stelter, P.: Stick-slip vibrations and chaos. *Philos. Trans. R Soc. London. Ser. A Phys. Eng. Sci.* **332**, 89–105 (1990). <https://doi.org/10.1098/rsta.1990.0102>
 48. Lima, R., Sampaio, R.: Stick–slip oscillations in a multi-physics system. *Nonlinear Dyn.* **100**, 2215–2224 (2020). <https://doi.org/10.1007/s11071-020-05677-5>
 49. Feynman, R.P.: The Feynman lectures on physics. Basic Books, New York (2013)
 50. Fang, H., Wang, K.W.: Piezoelectric vibration-driven locomotion systems – exploiting resonance and bistable dynamics. *J. Sound Vib.* **391**, 153–169 (2017). <https://doi.org/10.1016/j.jsv.2016.12.009>
 51. Szemplińska-Stupnicka, W., Rudowski, J.: Steady states in the twin-well potential oscillator: computer simulations and approximate analytical studies. *Chaos* **3**, 375–386 (1993). <https://doi.org/10.1063/1.165945>
 52. Elvin, N., Erturk, A.: Advances in energy harvesting methods. Springer, Cham (2013)

Publisher's Note Springer Nature remains neutral with regard to jurisdictional claims in published maps and institutional affiliations.